Microglial autophagy-associated phagocytosis is essential for recovery from neuroinflammation

Rasmus Berglund[1], Andre Ortlieb Guerreiro-Cacais[1], Milena Z. Adzemovic[1], Manuel Zeitelhofer[2], Harald Lund[1], Ewoud Ewing[1], Sabrina Ruhrmann[1], Erik Nutma[3], Roham Parsa[1], Melanie Thessen-Hedreul[1], Sandra Amor[3,4], Robert A. Harris[1], Tomas Olsson*[1] and Maja Jagodic*†[1]

[1]Department of Clinical Neuroscience, Karolinska Institutet, Center for Molecular Medicine, Karolinska University Hospital, 171 76 Stockholm, Sweden

[2]Division of Vascular Biology, Department of Medical Biochemistry and Biophysics, Karolinska Institutet, 171 65 Solna, Sweden

[3]Department of Pathology, Amsterdam UMC, Location VUmc, De Boelelaan 1117, 1081 HV Amsterdam, The Netherlands

[4]Centre for Neuroscience and Trauma, Blizard Institute, Barts and the London School of Medicine & Dentistry, Queen Mary University of London, United Kingdom

* Equal contribution

† Corresponding author

One sentence summary: Degradation of tissue debris and recovery from neuroinflammatory disease are impaired in *Atg7*-deficient microglia, a process mirrored by aging.

Abstract

Multiple Sclerosis (MS) is a leading cause of incurable progressive disability in young adults caused by inflammation and neurodegeneration in the central nervous system (CNS). The capacity of microglia to clear tissue debris is essential for maintaining and restoring CNS homeostasis. This capacity diminishes with age, and age strongly associates with MS disease progression, although the underlying mechanisms are still largely elusive. Herein, we demonstrate that the recovery from CNS inflammation in a murine model of MS is dependent on the ability of microglia to clear tissue debris. Microglia-specific deletion of the autophagy regulator *Atg7*, but not the canonical macroautophagy protein *Ulk1*, led to increased intracellular accumulation of phagocytosed myelin and progressive MS-like disease. This impairment correlated with a microglial phenotype previously associated with neurodegenerative pathologies. Moreover, *Atg7*-deficient microglia showed striking transcriptional and functional similarities to microglia from aged wild-type mice that were also unable to clear myelin and recover from disease. In contrast, induction of autophagy in aged mice using the disaccharide trehalose ubiquitously found in plant-based diets, led to functional myelin clearance and disease remission. Our results demonstrate that a non-canonical form of autophagy in microglia is responsible for myelin degradation and clearance leading to recovery from MS-like disease, and that boosting this process has a therapeutic potential for age-related neuroinflammatory conditions.

Introduction

Multiple Sclerosis (MS) is a chronic disease characterized by inflammation in the central nervous system (CNS) that triggers demyelination, glial cell dysfunction and irreversible neuro-axonal damage (*1*). While recent understanding of this immune dysfunction has led to the development of effective disease-modulatory treatments for inflammatory-active relapsing-remitting phase of MS, there is only one recently approved treatment for secondary progressive phase (*2*). Disease progression is not only the most clinically challenging aspect of MS, but it is the least mechanistically explored. Microglia activation, mitochondrial damage and ionic imbalance, among other mechanisms, have been associated with progressive neurodegeneration during MS (*3*).

Progressive MS exhibits a degenerative disease phenotype with glial cell dysfunction rather than infiltration of peripheral immune cells (*4*). In MS, microglia express an increased pro-inflammatory profile with both age and disease-burden (*4*). Age is the strongest risk factor for developing progressive MS (*5*). Many age-associated neurodegenerative pathologies such as Alzheimer's disease (AD) (*4, 6-8*), as well as autoinflammatory diseases including Crohn´s disease and Systemic Lupus Erythematosus (SLE) (*9, 10*), are characterized by impaired autophagy, a lysosomal degradation pathway used for removal of cellular constituents. Indeed, microglia surrounding MS lesions exhibit enhanced autophagy (*11*) and have the ability to phagocytose oligodendrocytes, as recently shown by single-nucleus RNA-sequencing (*12*). While among CNS myeloid cells microglia have been ascribed the highest phagocytic activity (*13*), the underlying mechanisms and their association with MS progression or tissue repair remain to be characterized.

Canonical autophagosome formation is highly dependent on the Unc-51-Like Kinase 1 (ULK1)-complex formation, as well as on Autophagy Related Protein 7 (ATG7) lipidation of LC3, the key component of autophagosomes. In addition, LC3 can also be conjugated to membranes of

phagosomes and endosomes, thereby facilitating the degradation of their cargo during processes termed LC3-associated phagocytosis and endocytosis, respectively (*14-16*), broadly referred to as non-canonical autophagy hereafter. Non-canonical autophagy is dependent on the protein RUBICON (*17*), which also inhibits the canonical autophagy pathway (*18*). Mutations in the *Rubicon* gene are associated with a familial form of ataxia with impaired lysosomal degradation (*19, 20*). Furthermore, inhibition of non-canonical autophagy in macrophages elicited by deletion of either *Atg7* or *Rubicon* causes an SLE-like disease in mice due to defective degradation of phagocytosed apoptotic cells (*21*). Similarly, specific impairment of non-canonical autophagy in microglia has been associated with reduced clearance of β-amyloid and progressive neurodegeneration in a murine model of AD (*16*), also evident in *Atg7* deficient mice (*22*). While targeting microglial autophagy in these diseases has been proposed to have great therapeutic potential (*8*), whether canonical or non-canonical autophagy impacts disease progression in MS is currently unknown.

We previously established a link between *Atg7* and disease severity in a common animal model of MS, experimental autoimmune encephalomyelitis (EAE) (*23*). Herein we pinpoint this effect to microglia, and we reveal how processing of myelin debris by microglia is dependent on ATG7 in a non-canonical form of autophagy. We further establish this process as a determinant of microglial phenotype in disease and aging and demonstrate how therapeutically inducing this pathway can restore CNS homeostasis.

Results

Microglial Atg7 deficiency prevents recovery from EAE

To investigate the association between *Atg7* and EAE, we deleted *Atg7* from two compartments highly relevant for disease pathogenesis, T cells and myeloid cells, using CRE recombinase expressed under *Lck* and *Lyz2* promoters, respectively (fig. S1). Deletion of *Atg7* in T cells did not affect clinical disease, although we did observe a previously reported reduction in $CD8^+$ T cell numbers (*24*) (fig. S1, A and B). In contrast, deletion of *Atg7* in *Lyz2*-expressing myeloid cells led to a persistent disease state that lacked the recovery evident in wild-type control mice (fig. S1C). $Lyz2^{Cre}$ targets several myeloid cell types including microglia (fig. S1D) (*22, 25, 26*), and the effect of *Atg7* deletion was restricted to the EAE recovery phase, suggesting CNS-intrinsic regulation. We detected the highest expression and most prominent *Atg7* u-regulation during EAE in $CD11b^+$ $CD45^{Int}$ cells (microglia) compared to other *Lyz2*-expressing CNS myeloid populations (Fig. 1A). Expression of the floxed *Atg7* exon 14 was dramatically reduced in microglia of $Atg7^{fl/fl}$ $Lyz2^{Cre}$ mice after EAE induction (fig. S1E). In addition, microglia from these mice displayed reduced lipidated membrane-bound LC3B (II) (fig. S1F), indicating less autophagosome formation and lysosomal loading of myelin after *in vitro* exposure (fig. S1G).

To test the hypothesis that microglial ATG7 plays a role in EAE progression, we utilized *Atg7* deletion under a tamoxifen-inducible CRE recombinase expressed under the *Cx3cr1* promoter. Tamoxifen-induced deletion is sustained in the self-renewing microglia population while other *Cx3cr1*-expressing cells essential for EAE such as monocytes and dendritic cells are derived from bone marrow precursors and repopulated from the bone marrow after 2-4 weeks (fig. S2A) (*27*). In all experiments, EAE was induced 4-8 weeks after tamoxifen treatment. Deletion of *Atg7* exon 14 in $Atg7^{fl/fl}$ $Cx3cr1^{CreERT2}$ microglia was confirmed at both 2 and 42 weeks after tamoxifen

administration (fig. S2B), as was reduced ATG7 protein expression (fig. S2C). *Atg7$^{fl/fl}$ Cx3cr1^{CreERT2}* mice exhibited a dramatic loss of recovery from EAE, confirming our hypothesis of a microglia-dependent phenotype (Fig. 1B).

Atg7 deficiency impacts microglial tissue debris clearance through non-canonical autophagy

As ATG7 is essential for both canonical and non-canonical autophagy (*14*, *17*), we compared phenotypes of *Atg7$^{fl/fl}$ Cx3cr1^{CreERT2}* mice with mice in which microglia were deficient in *Ulk1*, a protein only required for canonical autophagy (*21*). The *Ulk1$^{fl/fl}$ Cx3cr1^{CreERT2}* mice did not exhibit lack of recovery from EAE, suggesting that impaired non-canonical autophagy drives the disease phenotype in *Atg7$^{fl/fl}$ Cx3cr1^{CreERT2}* mice (Fig. 1C). This notion was further supported by the finding that microglia from both strains displayed reduced but comparable levels of starvation-induced canonical autophagy, as evident by decreased membrane-bound LC3B (II) (Fig. 1D) and increased IL-1β secretion and mitochondrial membrane potential (fig. S2, D and E). This reflects an impairment in typical canonical autophagy functions in securing mitophagy and inflammasome stability (*22*, *28-31*). In addition, we determined the key regulator of non-canonical autophagy, *Rubicon* (*17*), to accompany elevated *Atg7* expression in wild-type microglia after disease induction (Fig. 1E and table S1).

Deficiency in non-canonical autophagy has been associated with impaired degradation of bacterial proteins during infection as well as with impaired phagocytosis of apoptotic cells and β-amyloid, leading to SLE-like disease and AD, respectively (*16, 20-22, 32*). Indeed, *Atg7$^{fl/fl}$ Cx3cr1^{CreERT2}* microglia displayed a dramatically increased load of intracellular myelin detected *ex vivo* during EAE (Fig. 1F). The *ex vivo* EAE microglia also exhibited reduced autophagosome formation detected as membrane-bound intracellular LC3B (II) after selective digitonin

permeabilization (Fig. 1G). Immunofluorescence of microglia sorted 5 days after EAE induction, when microglia were activated but had not yet accumulated endogenous myelin load, confirmed the increased load of fluorescently-labeled myelin and decreased LC3 co-localization to myelin-containing vesicles in *Atg7$^{fl/fl}$ Cx3cr1^{CreERT2}* compared to *Ulk1$^{fl/fl}$ Cx3cr1^{CreERT2}* and wild-type control mice (Fig. 1H).

To further validate the impaired degradation of the phagocytosed debris in *Atg7* deficient microglia, we pulsed microglia with myelin stained with both a lipophilic dye (CellVue^{TM}) and a pH-sensitive dye (pHrodo^{TM}). Microglia were sorted *ex vivo* after immunization, circumventing the need for further stimulations, and we limited all incubations to ≤ 48h in order to minimize *in vitro* culture-induced changes of the microglial phenotype (*33*). We observed a decreased pHrodo^{TM} signal in *Atg7$^{fl/fl}$ Cx3cr1^{CreERT2}* microglia accompanied by increased CellVue^{TM} (Fig. 1I), indicating impaired degradation in *Atg7$^{fl/fl}$ Cx3cr1^{CreERT2}* microglia. This finding was further demonstrated using time-lapse imaging of microglia pulsed with labeled myelin, revealing an accumulation of phagocytosed myelin in *Atg7$^{fl/fl}$ Cx3cr1^{CreERT2}* microglia (Movie S1).

The impaired loading to degradation vesicles was also observed when *Atg7$^{fl/fl}$ Cx3cr1^{CreERT}* microglia were provided irradiated apoptotic CD171^{+} (neurons), GLAST^{+} (astrocytes) or O4^{+} (oligodendrocytes) cells (fig. S2F). Further analysis demonstrated a dramatically reduced clearance capacity of myelin debris from medium by microglia from *Atg7$^{fl/fl}$ Cx3cr1^{CreERT2}* compared to *Ulk1$^{fl/fl}$ Cx3cr1^{CreERT2}* and wild-type control mice following pulsed exposure to fluorescently-labeled myelin (Fig. 1J). Taken together, our data suggest that an impairment in microglial autophagy-associated degradation of phagocytosed myelin compromises the clearance of myelin debris leading to an inability to recover from MS-like disease.

Microglial Atg7 deficiency drives an altered transcriptional phenotype

To obtain a comprehensive overview of the consequences of *Atg7* deletion during EAE, we performed RNA sequencing of microglia sorted from naïve mice at 21- and 35-days post-induction of disease (p.i.). We detected 467 and 147 differentially expressed genes (DEG) (adj. p-value < 0.05, fold change > 1.5) between *Atg7*$^{fl/fl}$ *Cx3cr1*^{CreERT2} and littermate controls on days 21 and 35 p.i., respectively (table S1). Only 13 DEGs were detected (adj. p-value < 0.05, fold change > 1.5) between the genotypes in naïve microglia, suggesting that differences predominantly arise during EAE (table S1). We clustered DEGs ($p < 0.01$, fold change > 1.5) and then grouped the clusters based on their expression patterns (Fig. 2A), performing functional annotation of the groups using IPA, ORA and REViGO (*34*, *35*) (table S2). The first group (orange) represented changes considerably more pronounced in *Atg7*$^{fl/fl}$ *Cx3cr1*^{CreERT2} microglia that occurred early in disease (day 21 p.i.) and returned to levels in the naïve state by day 35 p.i. (Fig. 2A). These changes associated with pathways typical for activation of immune cells during EAE, such as IFN-γ-, STAT3- and GM-CSF-signaling, cell activation, expansion and migration (Fig. 2B). The second group (blue) represented genes that remained downregulated during disease, with *Atg7*$^{fl/fl}$ *Cx3cr1*^{CreERT2} microglia showing modest changes (Fig. 2A). Functionally, this group was enriched in pathways involved in myeloid cell function such as quantity, movement, and degranulation of myeloid cells, as well as activation of GATA2, which is important for the development of myeloid lineage cells (Fig. 2B). Genes in the third group (yellow) had a similar pattern to the first group in wild-type but not in *Atg7*$^{fl/fl}$ *Cx3cr1*^{CreERT2} microglia, which demonstrated the opposite pattern (Fig. 2A). These changes are predominantly associated with energy-related functions such as glycolysis and mitochondrial function, oxidative stress and cell adhesion (Fig. 2B and fig. S3). The fourth group (purple) represented genes that gradually increased their expression during disease

progression specifically in *Atg7*$^{fl/fl}$ *Cx3cr1*^{CreERT2} microglia (Fig. 2A). These genes are associated with cellular growth, including protein synthesis, EIF2- and mTOR-signaling, and were closely related to microglial development and function in CNS pathology (*36*) (Fig. 2B and fig. S3). The functional differences between the groups translated into differential disease enrichment, with early changes associating with inflammatory and infectious diseases, whereas changes in the progressive stage of EAE demonstrated strong enrichment in neurodegenerative diseases (Fig. 2C). These patterns resemble the course of MS, with the initial phase being dominated by inflammatory processes followed by neurodegeneration that, in later disease stages, becomes decoupled from the initial inflammation (*1*).

Atg7$^{fl/fl}$ *Cx3cr1*^{CreERT2} microglia exhibited pronounced but transient changes during early disease (Fig. 2, A and B, orange and yellow) that translated into altered microglia function and EAE development. These transcriptional profiles associated with immune cell activation and migration, reflected in increased microglia numbers and a more robust infiltration of bone marrow-derived macrophages (BMDMs), neutrophils, and T and B cells into the CNS parenchyma during early EAE (Fig. 3A). In accordance with IFN-γ and TNF predicted to be activated upstream regulators (Fig. 2B and table S2), a larger proportion of infiltrating T cells in *Atg7*$^{fl/fl}$ *Cx3cr1*^{CreERT2} mice were IFN-γ^{+} (fig. S4A). *Atg7*$^{fl/fl}$ *Cx3cr1*^{CreERT2} microglia themselves secreted dramatically larger amounts of IFN-γ, TNF and IL-1β (Fig. 3B), the latter suggesting activation of the inflammasome as previously reported to occur in response to myelin accumulation (*37*). Moreover, *Atg7*$^{fl/fl}$ *Cx3cr1*^{CreERT2} microglia were capable of stimulating T cell proliferation and expansion of pathogenic IFN-γ-producing cells *in vitro* (fig. S4, B-D). *Atg7* deficiency promoted a microglial phenotype that can augment inflammatory responses during EAE (fig. S4).

In MS patients, an increased inflammatory activity during the first 2 years after diagnosis has been associated with the risk of clinical progression during early disease (*38*). Long-term disability, nevertheless, better correlates with brain atrophy, reflecting neuro-axonal loss (*39, 40*). Interestingly, *Atg7* deletion resulted in a microglial phenotype that associated with neuronal function and neurodegenerative diseases (*4*), suggesting sustained transcriptional changes that are critical for disease progression (Fig. 2, A and C, purple). Indeed, a late stage transcriptional profile of *Atg7*$^{fl/fl}$ *Cx3cr1*^{CreERT2} microglia demonstrated a remarkable enrichment in microglial genes associated with neurodegenerative diseases (*4, 41*) and MS-associated microglia identified in recent single-cell RNA-sequencing studies (*42, 43*) (Fig. 3C, fig. S5 and table S3). We confirmed differences in protein levels of CLEC7A and CD11c/ITGAX (fig. S6A). In contrast, the homeostatic and tolerogenic state genes (*4, 44*) were depleted in *Atg7*$^{fl/fl}$ *Cx3cr1*^{CreERT2} microglia (Fig. 3C and fig. S5).

Microglia deficient in Atg7 have impaired signs of debris uptake and degradation

The *Clec7a* gene encodes the C-type lectin Dectin-1, which is known to induce LC3-associated phagocytosis and recognizes ligands released upon CNS damage (*45-48*). *Clec7a* expression characterizes a microglia population associated with neurodegenerative conditions (*4*). *Atg7*$^{fl/fl}$ *Cx3cr1*^{CreERT2} showed dramatically increased number of CLEC7A^{+} IBA1^{+} microglia compared to control mice (Fig. 3D and fig. S6B).

We observed that *Atg7* deletion did not affect the frequency of the CLEC7A^{int} population, but it did lead to a near loss of CLEC7A^{low} and a robust increase in CLEC7A^{high} cells (Fig. 3, E and F). CLEC7A^{high}, and in particular CLEC7A^{int}, microglial populations displayed dramatically lower surface expression of the scavenging receptors MSR1 (SR-A, CD204) (Fig. 3G), CD36 and

other receptors (e.g. CD200R, IA/IE) that are implicated in microglial function during inflammation (*49-51*) (fig. S6C). We further demonstrated that myelin phagocytosis relies, at least in part, on uptake mediated by MSR1, because the uptake of pHrodo-labelled myelin by microglia *in vitro* could be blocked using an MSR1 antibody (Fig. 3H), and myelin induced robust surface expression of MSR1 (Fig. 3I). Interestingly, whereas RNA-sequencing implicated an increased *Msr1* expression in *Atg7*$^{fl/fl}$ *Cx3cr1*^{CreERT2} microglia (fig. S6D), flow cytometry analysis revealed reduced surface receptor quantity (fig. S6E). A similar pattern was observed for CD36 (fig. S6, D and F). However, a pool of intracellular MSR1 was detected upon permeabilization (Fig. 3J), suggesting a blocking of retrograde trafficking of phagosomal receptors that has been described in the context of disrupted non-canonical autophagy (*16*). To confirm this we blocked the fusion of phagosomes and lysosomes in microglia *ex vivo* using Bafilomycin A1, which resulted in an increase in intracellular MSR1 and CD36 levels (Fig. 3I and fig. S6G). These data indicate that stalling myelin-loaded autophagosomes can lead to MSR1 retention that could further sustain microglial failure to clear myelin debris, as observed after repeated myelin pulsing (Fig. 1J). This pattern of intracellular accumulation in relation to myelin exposure and genotype was not detected upon targeting other potential myelin scavenger receptors such as CR3, CD16, CD64 or MARCO (fig. S6H).

Transcriptomic alterations of late stage microglia further supported the notion of impaired phagosomal degradation in *Atg7*-deficient microglia. A marked upregulation of apolipoprotein E (*Apoe*) was observed in late-stage *Atg7*$^{fl/fl}$ *Cx3cr1*^{CreERT2} microglia by RNA-sequencing (Fig. 3K), together with other lipoproteins (*Apoc1*, *Apoc4*) and lipoprotein lipase (*Lpl*) (fig. S6I). Upregulation of APOE occurs in response to the binding of myelin-derived cholesterol to the endogenous liver X receptor (LXR), which is transcriptionally activated in *Atg7*$^{fl/fl}$ *Cx3cr1*^{CreERT2}

243 microglia (Fig. 2B) and is crucial for the export of cholesterol from microglia to the extracellular
244 space (*37*). Moreover, we observed increased expression of *Apoe* when phagosome-lysosome
245 fusion was impaired using bafilomycin A treatment (Fig. 3K), again suggesting that *Apoe*
246 upregulation in *Atg7*$^{fl/fl}$ *Cx3cr1*^{CreERT2} microglia constitutes a response to intracellular myelin
247 accumulation. We also observed that TREM2, which can bind APOE and other lipids (*52*) and is
248 an inducer of the APOE pathway (*4*) and plays a major role in recovery from EAE (*53*), was
249 upregulated during late EAE stages (fig. S6J), and that the pathway of TREM2 was highly activated
250 (fig. S5). Finally, levels of TGF-β1, a marker of homeostatic microglia as opposed to LXR-APOE-
251 TREM2 disease-associated microglia (*4, 54*), was dramatically decreased in *Atg7*$^{fl/fl}$ *Cx3cr1*^{CreERT2}
252 microglia (Fig. 3L). *Atg7*$^{fl/fl}$ *Cx3cr1*^{CreERT2} microglia thus appear to cope with increase myelin load
253 by engaging the LXR-APOE-TREM2 pathway and by upregulating the expression of the MSR1
254 and other scavenging receptors to compensate for reduced retrograde transport and failed myelin
255 degradation.

256 Accumulation of myelin debris is a strong inhibitor of oligodendrocyte differentiation and
257 remyelination, suggested to hinder recovery from inflammatory insults during MS and EAE and
258 leads to neuro-axonal loss (*55, 56*). Indeed, staining of *Atg7*$^{fl/fl}$ *Cx3cr1*^{CreERT2} microglia *ex vivo* with
259 an antibody against degraded myelin basic protein (dMBP) revealed an accumulation of this protein
260 in late stage disease compared to microglia from control animals (Fig. 3M). Immunostaining of
261 spinal cords further demonstrated the accumulation of dMBP in tissue, which overlapped with areas
262 of activated microglia/infiltrating BMDMs (MAC3 bright) (Fig. 3N and fig. S7A). This was
263 accompanied by unresolved inflammation evident as increased representation of immune cells
264 during late stage EAE (fig. S7, B and C). Moreover, pulsing late stage *Atg7*$^{fl/fl}$ *Cx3cr1*^{CreERT2}
265 microglia with myelin *ex vivo* led to lower uptake as compared to microglia from control animals

(fig. S7D). We addressed whether the increased pool of tissue infiltrating BMDMs (fig. S7C) could compensate for the reduced phagocytic capacity in *Atg7*$^{fl/fl}$ *Cx3cr1*^{CreERT2} mice, but BMDM cells underperformed microglia in phagocytosis of myelin as assessed by both *ex vivo* myelin load in cells isolated from late disease stage as well as by an *in vitro* myelin clearance assay (fig. S7, D and E). Finally, flow cytometry assessment of oligodendrocytes isolated from the spinal cord at this time point confirmed a lower frequency of CD45^{-}GALC^{+}MOG^{+} myelinating cells in *Atg7*$^{fl/fl}$ *Cx3cr1*^{CreERT2} animals as compared to controls (fig. S7F). Accordingly, we recorded reduced myelination in the *Atg7*$^{fl/fl}$ *Cx3cr1*^{CreERT} late stage EAE spinal cords (fig. S7G). *Atg7*-dependent impairment of microglia needed to clear myelin upon an inflammatory demyelinating insult could not be compensated for by infiltrating phagocytes and was associated with reduced CNS myelination during late stage disease.

Aged microglia recapitulate the phenotype of young Atg7-deficient microglia

Since age is the strongest risk factor for progressive MS (*5, 57*) and as many age-associated neurodegenerative pathologies are characterized by impaired autophagy (*4, 6-8*), we compared the impact of *Atg7* deficiency in the context of aging. We observed a remarkable similarity between the transcriptomes of *Atg7*$^{fl/fl}$ *Cx3cr1*^{CreERT2} microglia and microglia from aged mice (> 80 weeks) compared to control young microglia (Fig. 4A and table S4). Both late disease stage microglia from *Atg7*$^{fl/fl}$ *Cx3cr1*^{CreERT2} mice and microglia from aged (> 80 weeks) wild-type mice revealed enrichment of genes associated with microglia during neurodegenerative diseases (*4, 41*), as well as MS-associated microglia (*42, 43*) (fig. S5). Accordingly, aged mice developed aggravated EAE with a clinical course similar to that of *Atg7*$^{fl/fl}$ *Cx3cr1*^{CreERT2} mice (Fig. 4B) and exhibited signs of accumulated myelin load (Fig. 4C). Similar to *Atg7*$^{fl/fl}$ *Cx3cr1*^{CreERT2}, *in vitro* time-lapse imaging

demonstrated that microglia from aged mice had reduced lysosomal loading of myelin as assessed by co-localization with low pH-sensing dye (pHrodo™) and the pH-indifferent dye (PKH26™), the latter detecting accumulation of myelin-containing phagosomes (Movie S2).

Trehalose boosts autophagy in aged microglia and promotes recovery from EAE

While increased understanding of the immune dysfunction during early relapsing-remitting phases of MS has led to the recent development of effective disease-modulatory treatments, progressive stages still largely lack treatment options. In accordance with our data, boosting microglial autophagy in neurodegenerative diseases has been proposed to have considerable therapeutic potential (*58-60*). However, whether this could have beneficial effects in MS, and whether canonical or non-canonical autophagy is involved in disease progression, is currently unknown. To target phagocytosed myelin through autophagy we administered trehalose, a disaccharide known to induce autophagy and ameliorate age-associated diseases (*61-66*). Daily trehalose administration starting 1 week before EAE induction led to a reduction in the clinical severity of EAE, and more than 40% of aged control mice recovered as well as aged *Ulk1*$^{fl/fl}$ *Cx3cr1*^{CreERT2} mice that have compromised canonical autophagy (Fig. 1D, Fig. 4B and fig. S8A). We did not observe any trehalose effect on clinical EAE in younger mice, regardless of the genotype, nor in aged *Atg7*$^{fl/fl}$ *Cx3cr1*^{CreERT2} mice (Fig. 4B and fig. S8A), suggesting that trehalose acts by boosting non-canonical autophagy. Indeed, we observed that trehalose increased nuclear density of TFEB, a key transcription factor for autophagy and lysosome-associated genes (*61*), and an increased formation of lysosomes defined by LAMP1, a major lysosome membrane component (Fig. 4D). We also detected increased expression of multiple autophagy and lysosome genes upon trehalose treatment of aged microglia (Fig. 4E).

Following trehalose treatment, we detected a reduction of intracellular microglial myelin load in aged EAE mice *ex vivo* (Fig. 4C), and increased myelin clearance and degradation through lysosomes *in vitro* (Fig. 4, F and G). Trehalose treatment also reduced the frequency of disease-associated microglia defined by expression of CLEC7A and APOE (Fig. 4H) as well as the infiltration of BMDMs (fig. S8B). Furthermore, microglia from trehalose-treated aged mice displayed reduced secretion of the disease-associated cytokines IFN-γ, TNF and IL-1β, and increased TGF-β1 secretion that reflected a normalization of the profile evident in microglia from young mice (Fig. 4I). Taken together we validated an age effect on autophagy-associated vesicular biogenesis, with a decline in lysosome loading of phagocytosed myelin debris, similar to that in *Atg7*$^{fl/fl}$ *Cx3cr1*^{CreERT2} microglia. In aged mice this impairment was successfully mitigated with trehalose treatment, with consequent effects on transcription, lysosome biogenesis, cytokine secretion and clinical disease outcome.

Discussion

We herein demonstrate that a non-canonical form of autophagy in microglia is responsible for myelin degradation and clearance and that impairment of this pathway, which occurs during aging, contributes to the progression of MS-like disease. Importantly, we show that we can modulate this process therapeutically, with implications in other age-related neuroinflammatory disease.

The cellular events underlying inflammatory bouts typical of MS and EAE are well characterized, while the events promoting resolution of inflammation and limiting progression are much less understood (*67*). However, accumulation of myelin and inflammatory debris in the target tissue are known factors with inhibitory effects on remyelination (*55, 56*). We now demonstrate that the impaired myelin clearance capacity of microglia leads to increased tissue deposits of myelin debris accompanied by reduced myelination and oligodendrocyte differentiation. The deletion of *Atg7* in microglia caused persistent neuroinflammation and, by comparing $Atg7^{fl/fl}$ $Cx3cr1^{CreERT2}$ mice with $Ulk1^{fl/fl}$ $Cx3cr1^{CreERT2}$, we demonstrated that the phenotype was largely independent from canonical autophagy. In several *in vivo* and *in vitro* experimental settings, we observed that the lack of *Atg7* drives microglial dysfunction in clearance and processing of myelin debris and apoptotic CNS cells. The reduced clearance capacity of the microglia is most likely a consequence of internalization of scavenger receptors due to impaired *Atg7*-dependent lysosomal degradation.

Our model presented an opportunity to study impaired degradation of phagocytosed components as a regulator of microglial phenotype, which is relevant for a broad range of myeloid cell-associated pathologies. The elevated infiltration of peripheral immune cells 21 days after EAE induction was associated with an altered $Atg7^{fl/fl}$ $Cx3cr1^{CreERT2}$ microglial cytokine profile, likely in synergy with increased myelin tissue deposits and local CNS expansion of immune cell

populations. Interestingly, the infiltrating macrophage population did not compensate for the reduced myelin clearance of *Atg7$^{fl/fl}$ Cx3cr1^{CreERT2}* mice. In fact, the capacity for myelin clearance of this population at a late disease stage was dramatically lower than that of microglia, which corroborates previous findings (*13*) and supports the established idea of microglia being promoters of homeostasis, in contrast to the monocyte-derived macrophages which exhibit a more inflammatory phenotype (*68*).

Although the day 21 EAE microglia of *Atg7$^{fl/fl}$ Cx3cr1^{CreERT2}* mice reflect an acute inflammatory state, the day 35 microglia represent a more unique phenotype relevant for evaluating the challenges of chronic inflammation and tissue degeneration. The microglial transcriptome from persistent EAE at day 35 in *Atg7$^{fl/fl}$ Cx3cr1^{CreERT2}* mice was similar to other reported disease-associated microglial transcriptomes, indicating shared microglial pathology (*4, 41*). Potentially pathogenic microglia are dependent on the TREM2-APOE axis (*4, 69*). In our *Atg7$^{fl/fl}$ Cx3cr1^{CreERT2}* day 35 EAE microglia, we observed an enriched TREM2 pathway accompanied by elevated *Apoe* expression *ex vivo* and *in vitro* as a consequence of increased intracellular myelin load. Intracellular lipids are sensed by LXR which acts as a transcription factor inducing *Apoe* expression. We propose an LXR-mediated pathogenic feed-forward mechanism through APOE in which intracellular myelin is not functionally degraded. The enriched LXR pathway in *Atg7$^{fl/fl}$ Cx3cr1^{CreERT2}* microglia resembled the macrophage phenotype characteristic of atherosclerosis, a disease state in which there is pathogenic accumulation of intracellular lipid compounds (*64*).

Phagocytosis of tissue debris has been reported to be essential for the maintenance of tissue homeostasis (*70*), and we demonstrate that upon inflammation the re-establishment of an anti-inflammatory response and subsequent tissue recovery are curbed when phagocytosis is decoupled from downstream cargo degradation through non-canonical autophagy. Expression of molecules

associated with disease states (e.g. CLEC7A, CD11c) was increased in *Atg7*$^{fl/fl}$ *Cx3cr1*^{CreERT2} microglia while the expression of genes that characterize homeostatic microglia was reduced (e.g. P2Ry12, CSF1R, CD200R, MSR1, TGF-β1) (*54*). Among these, CLEC7A is of great interest as it is a strong inducer of LC3-associated phagocytosis (*47, 48*). Elevated expression of CLEC7A reported here for EAE and previously associated with pathology-associated microglia in other models (*4*) is therefore directly linked to an important functional outcome.

Increased age leads to a decline in autophagy and is a risk factor for progressive MS and neurodegeneration (*57, 71*). Dysfunctional aged myeloid cells have been reported in other settings to be a consequence of inefficient autophagy (*72*). We thus explored the potential of induced autophagy in ameliorating age-associated aggravated EAE disease. Treatment with the autophagy-inducing disaccharide trehalose led to a robust recovery rate and decline in clinical symptoms in aged mice, reminiscent of the recovery characteristic of untreated young wild-type mice (*65, 73*). However, trehalose treatment did not affect recovery of young wild-type mice or *Atg7*$^{fl/fl}$ *Cx3cr1*^{CreERT2} mice, suggesting that non-canonical autophagy in microglia from young mice is already at sufficient capacity, and that the effect of trehalose treatment in aged mice is dependent on microglial ATG7, regardless of whether trehalose exerts its effect upstream or downstream of ATG7. The trehalose treatment induced vesicle biogenesis through transition of transcription factor TFEB to the nucleus, increased lysosome density and myelin clearance and degradation. Trehalose treatment *in vivo* also reduced the density of CNS infiltrating bone marrow-derived macrophages during EAE and a reduced pro-inflammatory cytokine profile evident in microglia from aged mice.

The tools for defining and studying microglia have developed vastly over the past years, allowing for more accurate *ex vivo* and *in vitro* experiments, which however have an impact on the microglial phenotype, especially regarding contextual and dynamic processes such as autophagy.

Another challenge for future work is the characterization of autophagy-associated phagocytosis in humans, especially in disease context as in progressive human neuroinflammation. Additional work on molecules of the microglial autophagy-associated phagocytosis including RUBICON would also add support to our findings and could unveil interesting pharmacological targets. Finally, the phenotypes observed on autophagy-deficient microglia could partially stem from secondary effects such as increased phagosome load which also warrants further exploration.

Taken together our findings demonstrate that degradation of inflammatory myelin debris by microglia is dependent on the non-canonical arm of autophagy, a function necessary for cell and CNS tissue homeostasis. We thus provide a functional link between age, autophagy and myeloid dysfunction. We associate our phenotype with the newly described microglial transcriptomes primarily described in neurodegenerative diseases, suggesting a shared pathology and providing a functional characterization. Finally, we propose this pathway to be as a promising treatment target for age-associated CNS pathology.

Materials and Methods

Study design

Previous work by our lab established a link between *Atg7* and disease severity in EAE, an animal model for MS (*23*). In this study, we set out to understand whether this effect was intrinsic to the immune system by broadly targeting the deletion of *Atg7* in mice to either T cells or myeloid cells by crossing *Atg7*-floxed mice to Lck^{CRE} or $Lyz2^{CRE}$ expressing strains, respectively. Since the effect of the deletion was observed during the recovery phase of EAE, which pointed to effects within the CNS, we further restricted *Atg7* deletion to microglia and CNS-resident macrophage populations by crossing *Atg7*-floxed mice to a $Cx3cr1^{CreERT2}$ expressing strain (see Experimental subjects section). Experiments were performed with littermate controls, using both males and females. Animals were randomized and the majority of analysis was done in a blinded fashion. Sample sizes varied depending on the goal of each experiments (i.e. dissection at one or multiple timepoints, *in vitro* cultures, etc.) and expected effect sizes, and numbers of animals as well as statistical analysis methods are thus given in each figure for every experimental setup. No animals were excluded from analyses apart from two samples in RNA-sequencing that did not have correct genotype. Catalogue numbers and the description of different primers, antibodies and kits used throughout the study can be found as an additional technical sheet (table S5).

Ethics Statement

Animal experiments were approved and performed in accordance with the guidelines from the Swedish National Board for Laboratory Animals and the European Community Council Directive (86/609/EEC) under the ethical permits N284/07 (N332/06), N338/, N138/14, N1387/14 and 9328-

2019 which were approved by the North Stockholm Animal Ethics Committee (Stockholms Norra djurförsöksetiska nämnd). Mice were tested according to a health-monitoring program at the National Veterinary Institute (Statens Veterinärmedicinska Anstalt, SVA) in Uppsala, Sweden.

Experimental Subjects

Gene-deleted mice on the C57BL/6 background were generated by cross-breeding of *Atg7*$^{fl/fl}$ or *Ulk1*$^{fl/fl}$ to *Lck*^{CRE}, *Lyz2*^{CRE} or *Cx3cr1*^{CreERT2} transgenic mice. All strains were purchased from The Jackson Laboratory except *Atg7*$^{fl/fl}$ that was a gift from Dr. Klas Blomgren. All experimental Cre mice had a hemizygote genotype. *Cx3cr1*^{CreERT2} mice were treated with 4mg tamoxifen (TAM; Sigma), dissolved in corn oil and administrated subcutaneously three times, at 48-hour intervals. Experiments were initiated at earliest 4 weeks after the first tamoxifen administration to allow for repopulation of peripheral bone marrow-derived *Cx3cr1*^{CreERT2} expressing cells such as monocytes, while the gene deletion effect is preserved in the self-renewing CNS resident microglial population. While border associated macrophages in meninges and perivascular spaces also express *Cx3cr1*, self-renew and are targeted by TAM administration, they have been shown not to contribute to T cell activation and CNS damage during EAE and are absent in the parenchyma where the processes of myelin uptake and degradation described in this paper occur(*74, 75*). No dramatic influence from the *Atg7*$^{fl/fl}$ allele or Cre$^{+/-}$ toxicity was observed. In EAE experiments, 10-18 weeks old littermate mice were used. Aged mice were > 80 weeks old.

Induction and Clinical Evaluation of EAE

Recombinant mouse myelin oligodendrocyte glycoprotein (rmMOG) aa1-125 from the N-terminus, was expressed in *Escherichia coli* and purified to homogeneity using chelate

chromatography, as previously described(*76, 77*). The purified protein, dissolved in 6M urea, was dialyzed against PBS. For EAE induction mice were immunized with a single subcutaneous injection at the dorsal tail base with 100µl of inoculum containing rmMOG, 18-30µg/mouse in saline solution emulsified in a 1:1 ratio with Complete Freund's Adjuvant (CFA, Chondrex) (100µg *Mycobacterium tuberculosis*/mouse), all under isoflurane (Baxter) anesthesia. Additionally, all experimental animals received an i.p. injection of 200ng/mouse pertussis toxin (PTX, Calbiochem) at days 0 and 2 p.i.

The clinical score was graded as follows: 0, no clinical signs of EAE; 1 - tail weakness or tail paralysis; 2 - hind leg paraparesis or hemiparesis; 3 - hind leg paralysis or hemiparalysis; 4 - tetraplegia or moribund; 5 - death. EAE remission was calculated as number of mice with full recovery (score 0) divided by total EAE incidence within the subgroup.

Single cell suspensions from CNS

CNS cells were extracted using the Neural Tissue dissociation kit T (Miltenyi Biotech). Mice were anesthetized with isoflurane and transcardially perfused with ice-cold PBS. Brains and spinal cords were mechanically minced and resuspended in enzyme mix according to the manufacturer's protocol. The CNS homogenates were then passed through a 40µm cell strainer and washed with PBS containing 5mM Ethylenediaminetetraacetic acid (EDTA). The pellet was resuspended in a 38% Percoll (Sigma) solution and centrifuged at 800g for 15 min (no brake). The myelin gradient layer was extracted and cells resuspended in PBS.

Cell cultures

Cells were cultured in Dulbecco's modified Eagles medium (DMEM, Sigma) conditioned with Fetal bovine serum 10% (vol/vol) (FBS, Sigma) and Penicillin/Streptomycin 1% (vol/vol) (Sigma) and M-CSF 20ng/ml (R&D). For the starvation-induced autophagy experiment cells were kept in Earle's balanced salt solution (EBSS, Sigma) for 5h before analysis. Bafilomycin A1 (Sigma) was used in concentration of 1μM.

Flow cytometry

CNS cells were analyzed at several time points from naive to day 35 p.i. EAE. Single-cell suspensions were plated and stained with conjugated antibodies and LIVE/DEAD™ Fixable Near-IR Dead Cell Stain (Invitrogen; L34976). Intracellular/Intranuclear staining was performed after permeabilization using a Fixation/Permeabilization kit (BD biosciences/eBioscience). LC3 was detected using a digitonin kit causing mild permeabilization, leaving mainly membrane-bound LC3 in the cell for analysis. Mitochondrial membrane potential was quantified using the Mitotracker deep red^{TM} probe. Cells were acquired using a Gallios flow cytometer (Beckman Coulter) and analyzed using Kaluza software (Beckman Coulter). All antibodies and reagents are specified in the enclosed technical data file.

Cell sorting

Cells from mouse CNS were sorted using a BD Influx cell sorter. Microglia were sorted as Live, $CD11b^+$ $CD45^{Intermediate(Int)}$ $Ly6G^-$ and/or $eYFP^+$ (fig. S9). Bone marrow-derived macrophages were sorted as Live $CD11b^+$ $CD45^{High}$ $Ly6G^-$ and/or $eYFP^-$. Neutrophils were sorted as Live $CD11b^+$ $Ly6G^+$ and/or $eYFP^-$. Cells for some *in vitro* experiments were sorted from naïve or day 5 p.i. mouse CNS using CD11b magnetic beads and columns (MACS, Miltenyi Biotech). Purity was determined using flow cytometry to be > 90% YFP^+ cells. The purpose of sorting cells from day 5

p.i. was to acquire activated microglia without accumulated intracellular myelin phagosomes. Blood monocytes were sorted using Ly6C magnetic beads (MACS, Miltenyi Biotech).

Mouse cell RNA, cDNA preparation and Expression Analysis

Cell pellets from sorted mouse CNS cells were lysed in RLT buffer and RNA extracted using a RNeasy mini kit (Qiagen). Reverse transcription of total RNA was performed using random hexamer primers (Invitrogen) and Superscript Reverse Transcriptase (Invitrogen). cDNA was stored at -20°C until use. qPCR was performed in triplicates using a CFX384™ Real-Time PCR Detection Systems with SYBR green as fluorophore (Bio-Rad). C(t) values with inter-duplicate differences more than one cycle were excluded. Target expression was calculated using the Bio-Rad CFX Manager V1.6. software. *Hprt* or the geometrical mean of *Gapdh* and *Hprt* was used as housekeeping gene reference.

Next-generation sequencing

Sorted microglia were pooled 1:1 female and male. RNA was prepared using a RNeasy Mini Kit (Qiagen) followed by quality control assessed with a Bioanalyzer 2100 (Agilent). All samples included had high quality RNA (RIN = 8.5–10). RNA was amplified with a SMARTer Stranded Total RNA-Seq Kit–Pico Input Mammalian (Clontech). Next-generation sequencing and generation of bioinformatic data was performed by the National Genomics Infrastructure (NGI) at the Science for Life Laboratory using a HiSeq 2500 System with a HiSeq Rapid SBS Kit v2 (Illumina). Data normalization and analysis of differential gene expression were performed using the DESeq2 R package with a negative binomial test(*78*). The false-discovery-rate-adjusted P value was estimated using the Benjamini–Hochberg correction(*79*). Data was further analyzed using

Ingenuity pathway analysis (IPA, Qiagen) and Gene set enrichment analysis (GSEA, Broad institute). GSEA analysis performed with standard settings – Classic scoring scheme for the enrichment score signal2noise metrics for the ranked gene list. Heat maps show in different figures show the range of expression values in red – blue (denoting high - low) calculated from normalized counts.

Myelin isolation and staining

Pure myelin was obtained using a protocol adapted from Norton and Poduslo (*80*). Briefly, myelin was isolated through mechanical homogenization of perfused brains in homogenization buffer with PBS containing 0.32M sucrose. After two washes in homogenization buffer, an 0.85M sucrose solution in PBS underlay was added to the CNS homogenate. The CNS gradient was centrifuged at 4500g for 50 min. The interphase containing myelin was then washed twice in water. The purified myelin was then incubated with pHrodo dye and/or CellVue™ Plum and /or Fluoromyelin™ (all from Thermo Fischer Scientific) and/or PKH26™ (Sigma) in PBS/Hepes according to the manufacturer's instructions, followed by washing.

Immunofluorescence

CNS cells were sorted and plated into poly-L-lysine coated plates and incubated for 36h before adding purified myelin for an additional 12h. After washing, cells were fixed with 4% PFA and permeabilized with 0.2% Tween-20. Non-specific binding was blocked by adding 10% BSA and serum from secondary antibody producing species. Cells were then incubated overnight with primary antibodies diluted in PBS containing 1% BSA and 0.2% Tween-20. After washing, secondary antibodies diluted in host serum were added and incubated at 37°C for 1 h. Finally,

DAPI solution (4′,6-Diamidino-2-Phenylindole, Dihydrochloride, 0.2μg/ml, BD Biosciences) was added to the wells for 3 min before final washing. Samples were analyzed using a Leica Confocal microscope and Leica LAS-X software. Cellprofiler™ (Broad institute) software was used for quantitative analysis (analysis pipeline enclosed). Images were acquired using the same settings for all samples.

Phagocytosis assays

Phagocytic uptake and loading to low pH lysosomes were quantified by flow cytometry analysis of *ex vivo* CNS cells or sorted *in vitro* myeloid populations. For apoptotic cell phagocytosis panels CNS cells were sorted using MACS™ kits for either CD171, O4 or GLAST (Miltenyi biotech). Apoptosis was induced by radiation using a Precision X-rad (1Gy/min at 320KV, 12.5mA) twice with 8 h incubation pause (Li et al., 1996). pHrodo™ labeled cells were pulsed with stained myelin or apoptotic cells for 30 min followed by washing and flow cytometry.

Incucyte time-lapse imaging

Sorted microglia were pulsed with purified myelin stained with pHrodo Green and PKH26. Incubation plates were immediately transferred to an incubator connected to an Incucyte ZOOM™ instrument in which wells were analyzed using 20x ocular magnification every hour for 16-28h, generating time-lapse movies. (Green: Excitation Wavelength: 460 nm, Emission Wavelength: 524 nm. Red: Excitation Wavelength: 585 nm, Emission Wavelength: 635 nm)

LC3B-II detection and Digitonin permeabilization protocol

Membrane-bound lipidated LC3 (II) was detected after mild digitonin permeabilization extracting cytosolic LC3 according to a previously described protocol(*81*). Cells seeded in 96 well plates were treated with the non-ionic detergent Digitonin (Sigma) at a concentration of 50μg/mL in PBS for 5 min at room temperature. This permeabilizes the membrane for extracellular diffusion of non-bound LC3 while membrane-bound LC3 remains in the autophagosomal membrane. Cells were then fixed in 4% (w/vol) paraformaldehyde/PBS for 10 min at room temperature. After two washes in PBS, cells were incubated with an anti-LC3B antibody for detecting membrane-bound LC3B.

Acid wash stripping of surface molecules

Analysis of receptor internalization was achieved using a protocol for acid-wash stripping of surface receptors. Cultured cells were detached with EDTA and incubated with PBS containing glycine (100mM) and NaCl (150mM) (pH 2.5) for 5 min on ice. Cells were then stained and analyzed by flow cytometry after fixation with or without permeabilization.

Myelin clearance assay

Sorted *ex vivo* microglia from immunized mice (day 5 or 21 p.i.) were seeded at $5x10^4$ cells per well in 96 well plates and incubated for 12 h before PKH26- conjugated myelin was added. At the indicated timepoints, supernatant was removed and analyzed using a SpectraMax 384 microplate reader for fluorescence at 560nm. The remaining myelin concentration was determined in relation to a standard dilution series.

Microglia-CD4 T-cell co-culture

Sorted *ex vivo* microglia from immunized mice (day 5 p.i.) were seeded at $2\ x10^4$ cells per well in

96 well plates coated with poly-L-lysine. After 24 h, 2 x10^4 MACS-sorted $CD4^+$ T cells (Miltenyi Bioscience) from EAE mice (day 21 p.i.) were added per well. After 36 h cells, cells were analyzed by flow cytometry after intranuclear Ki67 labeling as a marker of proliferation.

ELISA

Sorted *ex vivo* microglia from naive mice and mice during EAE were incubated in DMEM, (Sigma) conditioned with Fetal bovine serum 10% (vol/vol) (FBS, Sigma) and penicillin/streptomycin 1% (vol/vol) for 24h in 96 well plates. Supernatants were collected and cytokine production was quantified using ready-set-go ELISA kits (eBioscience, Invitrogen) and a SpectraMax 384 microplate reader plate reader according to the manufacturer's instructions.

Trehalose treatment of EAE

For studies of the clinical effects of trehalose, mice were treated with water supplemented with either 5% (w/vol) D-(+)-trehalose dihydrate or 5% (w/vol) sucrose (both from Sigma) starting at the day of immunization. Sucrose was used as control given its similarity to trehalose since both are disaccharides, thus excluding elevated calorie availability as a determinant of EAE recovery. I.p. injections of 20% (w/vol) trehalose, 20% (w/vol) sucrose, 20% (w/vol) or PBS supplemented the treatment every third day starting from EAE onset until end of experiment. During severe EAE, mice were fed with trehalose, sucrose and water at a final concentration of 20% (w/vol). The i.p. doses were equal to previously reported clinical experiments while the drinking water was enriched to 5% (w/vol) trehalose (compared to 3% (w/vol) (*62*). This was a result of a titration experiment using 0, 3, and 5% (w/vol) with a stronger impact evident with the higher dose.

612 **Trehalose and TFEB *in vitro* assays**

613 *Ex vivo* microglia were cultured in medium with or without D-(+)-trehalose dihydrate at a final
614 concentration of 3% (w/vol). ICC experiments were performed as described above using
615 antibodies against TFEB (Rabbit, Bethyl, diluted 1:1000) and LAMP1 (Rat, Sigma, diluted
616 1:1000), which labels lysosomes, and secondary antibodies Alexa fluor 647 goat anti-rat (Thermo
617 fisher) and goat-anti rabbit Alexa fluor 546 (Thermo fisher), respectively. TFEB and $LAMP1^{+}$
618 lysosomes were quantified in relation to DAPI-defined nuclei (0.2 μg/ml) using Cellprofiler™
619 software.

620

621 **Histopathology and immunofluorescence (IF)**

622 Histopathological and IF analyses were performed on 3–5 μm thick paraffin-embedded spinal cord
623 cross-sections. Luxol fast blue (Kluever; Sigma) was used to assess tissue
624 demyelination. Quantitative evaluation of demyelination presented as the demyelination score
625 (DM) was performed on an average of 7 complete cross-sections of the spinal cord per mouse, as
626 previously described by Storch *et al.* (Storch et al., 1998). All images were captured using a Leica
627 Polyvar 2 microscope.

628 For IF analyses, the paraffin-embedded spinal cord cross-sections were treated as previously
629 described(*82*). After deparaffinization in xylol, sections were transferred to 90% (vol/vol) ethanol.
630 Endogenous peroxidase was blocked by incubation in methanol with 0.02% H_2O_2 for 30 min at RT
631 and rehydration to distilled water followed via a 90% (vol/vol), 70% (vol/vol), and 50% (vol/vol)
632 ethanol series. Antigen retrieval was performed with Dako target retrieval solution (Dako) for 1 h
633 in a steamer device at 98°C. Sections were subsequently incubated in 10% FCS in PBS for 30 min
634 at RT before incubation with the primary antibody on 4°C, overnight. Primary antibodies used in

costainings were Mac3 (Rat, BD Biosciences, diluted 1:200), dMBP (Rabbit, Millipore diluted, 1:200), CLEC7A (Rabbit, Abcam, diluted 1:500) and YFP (Chicken, Abcam, diluted 1:200), CD45 (Rat, BD Biosciences, diluted 1:200), CLEC7A (Rabbit, Abcam diluted 1:200). After washing in PBS, sections were incubated with a secondary antibody for 1 h at RT. Secondary antibodies were used in the following combinations: Alexa Fluor 555 donkey anti-rat IgG (Abcam), Alexa Fluor 488 donkey anti-rabbit IgG (Abcam) or rabbit anti-chicken IgY FITC (Thermo fischer), respectively. DAPI (0.2µg/ml) was included in the last washing step to visualize the nuclei. All images were acquired using Zeiss LSM700 confocal microscope and the ZEN 2009 software. Representative images shown are maximum intensity projections of 3µm thick z-stacks. Quantifications of the specific immunoreactivity was performed on five whole spinal cord cross-sections per mouse using ImageJ64, based on the number of pixels above an estimated threshold.

Statistical Analysis

GraphPad Prism 8 (http://www.graphpad.com/) was used for all the statistical analysis. In graphs with several comparisons, a dotted line separates the datasets that were compared. All figure legends include information regarding statistical tests used and sample size.

Supplementary materials

Fig. S1. Recovery from experimental autoimmune encephalomyelitis (EAE) requires functional autophagy in the myeloid but not in the T cell compartment.

Fig. S2. *Atg7* and *Ulk1* deficiency in microglia impact non-canonical and canonical autophagy, respectively.

Fig. S3. *Atg7* deficiency induces alterations in microglial transcriptome during experimental autoimmune encephalomyelitis (EAE).

Fig. S4. *Atg7* deficiency in microglia increases T cell proliferation and polarization to an inflammatory phenotype.

Fig. S5. Gene-set enrichment analysis.

Fig. S6. *Atg7* deficient microglia have impaired scavenger receptor recirculation associated with increased inflammation and a reduced myelinating oligodendrocyte population in experimental autoimmune encephalomyelitis (EAE).

Fig. S7. Late stage experimental autoimmune encephalomyelitis (EAE) is characterized by extensive tissue destruction and signs of increased in inflammation in mice with *Atg7*-deficient microglia.

Fig. S8. Trehalose boosts experimental autoimmune encephalomyelitis (EAE) recovery and decreases immune infiltration in aged mice.

Fig. S9. Gating strategy for defining cell populations by flow cytometry.

Table S1. RNAseq data (Excel)

Table S2. IPA, ORA and REVIGO analysis (Excel)

Table S3. Genes shared among homeostatic or pathogenic gene sets (Excel)

Table S4. RNAseq data (Excel)

Table S5. Technical data file (Excel)

Table S6. Raw data (Excel)

Movie S1. Accumulation of phagocytosed myelin in *Atg7*$^{fl/fl}$ *Cx3cr1*^{CreERT2} microglia

Movie S2. Accumulation of myelin-containing phagosomes in microglia of aged mice

References

1. M. Filippi *et al.*, Multiple sclerosis. *Nat Rev Dis Primers* **4**, 43 (2018).
2. L. Kappos *et al.*, Siponimod versus placebo in secondary progressive multiple sclerosis (EXPAND): a double-blind, randomised, phase 3 study. *Lancet* **391**, 1263-1273 (2018).
3. D. H. Mahad, B. D. Trapp, H. Lassmann, Pathological mechanisms in progressive multiple sclerosis. *Lancet Neurol* **14**, 183-193 (2015).
4. S. Krasemann *et al.*, The TREM2-APOE Pathway Drives the Transcriptional Phenotype of Dysfunctional Microglia in Neurodegenerative Diseases. *Immunity* **47**, 566-581.e569 (2017).
5. A. Scalfari, A. Neuhaus, M. Daumer, G. C. Ebers, P. A. Muraro, Age and disability accumulation in multiple sclerosis. *Neurology* **77**, 1246-1252 (2011).
6. K. Blennow, M. J. de Leon, H. Zetterberg, Alzheimer's disease. *Lancet* **368**, 387-403 (2006).
7. D. C. Rubinsztein, G. Marino, G. Kroemer, Autophagy and aging. *Cell* **146**, 682-695 (2011).
8. M. S. Uddin *et al.*, Autophagy and Alzheimer's Disease: From Molecular Mechanisms to Therapeutic Implications. *Front Aging Neurosci* **10**, 04 (2018).
9. M. R. Spalinger, G. Rogler, M. Scharl, Crohn's disease: loss of tolerance or a disorder of autophagy? *Dig Dis* **32**, 370-377 (2014).
10. X. Liu, H. Qin, J. Xu, The role of autophagy in the pathogenesis of systemic lupus erythematosus. *Int Immunopharmacol* **40**, 351-361 (2016).

11. G. P. Parnell, D. R. Booth, The Multiple Sclerosis (MS) Genetic Risk Factors Indicate both Acquired and Innate Immune Cell Subsets Contribute to MS Pathogenesis and Identify Novel Therapeutic Opportunities. *Frontiers in Immunology* **8**, (2017).

12. L. Schirmer *et al.*, Neuronal vulnerability and multilineage diversity in multiple sclerosis. *Nature*, (2019).

13. B. A. Durafourt *et al.*, Comparison of polarization properties of human adult microglia and blood-derived macrophages. *Glia* **60**, 717-727 (2012).

14. J. Martinez *et al.*, Microtubule-associated protein 1 light chain 3 alpha (LC3)-associated phagocytosis is required for the efficient clearance of dead cells. *Proceedings of the National Academy of Sciences of the United States of America* **108**, 17396-17401 (2011).

15. M. Komatsu *et al.*, Impairment of starvation-induced and constitutive autophagy in Atg7-deficient mice. *The Journal of cell biology* **169**, 425-434 (2005).

16. B. L. Heckmann *et al.*, LC3-Associated Endocytosis Facilitates beta-Amyloid Clearance and Mitigates Neurodegeneration in Murine Alzheimer's Disease. *Cell* **178**, 536-551 e514 (2019).

17. J. Martinez *et al.*, Molecular characterization of LC3-associated phagocytosis reveals distinct roles for Rubicon, NOX2 and autophagy proteins. *Nature cell biology* **17**, 893-906 (2015).

18. S. Nakamura *et al.*, Suppression of autophagic activity by Rubicon is a signature of aging. *Nature communications* **10**, 847 (2019).

19. M. Assoum *et al.*, The Salih ataxia mutation impairs Rubicon endosomal localization. *Cerebellum (London, England)* **12**, 835-840 (2013).

20. S. W. Wong, P. Sil, J. Martinez, Rubicon: LC3-associated phagocytosis and beyond. *The FEBS journal* **285**, 1379-1388 (2018).

21. J. Martinez *et al.*, Noncanonical autophagy inhibits the autoinflammatory, lupus-like response to dying cells. *Nature* **533**, 115-119 (2016).

22. M. H. Cho *et al.*, Autophagy in microglia degrades extracellular beta-amyloid fibrils and regulates the NLRP3 inflammasome. *Autophagy* **10**, 1761-1775 (2014).

23. M. Thessen Hedreul *et al.*, Combining genetic mapping with genome-wide expression in experimental autoimmune encephalomyelitis highlights a gene network enriched for T cell functions and candidate genes regulating autoimmunity. *Human molecular genetics* **22**, 4952-4966 (2013).

24. H. H. Pua, J. Guo, M. Komatsu, Y. W. He, Autophagy is essential for mitochondrial clearance in mature T lymphocytes. *Journal of immunology (Baltimore, Md. : 1950)* **182**, 4046-4055 (2009).

25. L. Batti *et al.*, TMEM16F Regulates Spinal Microglial Function in Neuropathic Pain States. *Cell Rep* **15**, 2608-2615 (2016).

26. H. Gao *et al.*, Metal transporter Slc39a10 regulates susceptibility to inflammatory stimuli by controlling macrophage survival. *Proceedings of the National Academy of Sciences of the United States of America* **114**, 12940-12945 (2017).

27. C. N. Parkhurst *et al.*, Microglia promote learning-dependent synapse formation through brain-derived neurotrophic factor. *Cell* **155**, 1596-1609 (2013).

28. Z. Zhong *et al.*, NF-kappaB Restricts Inflammasome Activation via Elimination of Damaged Mitochondria. *Cell* **164**, 896-910 (2016).

29. M. Kundu *et al.*, Ulk1 plays a critical role in the autophagic clearance of mitochondria and ribosomes during reticulocyte maturation. *Blood* **112**, 1493-1502 (2008).
30. J. Zhang *et al.*, Mitochondrial clearance is regulated by Atg7-dependent and -independent mechanisms during reticulocyte maturation. *Blood* **114**, 157-164 (2009).
31. H. She, Y. He, Y. Zhao, Z. Mao, Release the autophage brake on inflammation: The MAPK14/p38alpha-ULK1 pedal. *Autophagy* **14**, 1097-1098 (2018).
32. A. Gluschko *et al.*, The beta2 Integrin Mac-1 Induces Protective LC3-Associated Phagocytosis of Listeria monocytogenes. *Cell host & microbe* **23**, 324-337.e325 (2018).
33. C. Caldeira *et al.*, Microglia change from a reactive to an age-like phenotype with the time in culture. *Frontiers in cellular neuroscience* **8**, 152 (2014).
34. B. Zhang, S. Kirov, J. Snoddy, WebGestalt: an integrated system for exploring gene sets in various biological contexts. *Nucleic Acids Res* **33**, W741-748 (2005).
35. F. Supek, M. Bosnjak, N. Skunca, T. Smuc, REVIGO summarizes and visualizes long lists of gene ontology terms. *PLoS One* **6**, e21800 (2011).
36. T. K. Ulland *et al.*, TREM2 Maintains Microglial Metabolic Fitness in Alzheimer's Disease. *Cell* **170**, 649-663 e613 (2017).
37. L. Cantuti-Castelvetri *et al.*, Defective cholesterol clearance limits remyelination in the aged central nervous system. *Science (New York, N.Y.)* **359**, 684-688 (2018).
38. E. Leray *et al.*, Evidence for a two-stage disability progression in multiple sclerosis. *Brain* **133**, 1900-1913 (2010).
39. M. Filippi *et al.*, Gray matter damage predicts the accumulation of disability 13 years later in MS. *Neurology* **81**, 1759-1767 (2013).

40. M. A. Rocca *et al.*, Long-term disability progression in primary progressive multiple sclerosis: a 15-year study. *Brain* **140**, 2814-2819 (2017).
41. H. Keren-Shaul *et al.*, A Unique Microglia Type Associated with Restricting Development of Alzheimer's Disease. *Cell* **169**, 1276-1290.e1217 (2017).
42. T. Masuda *et al.*, Spatial and temporal heterogeneity of mouse and human microglia at single-cell resolution. *Nature* **566**, 388-392 (2019).
43. L. Schirmer *et al.*, Neuronal vulnerability and multilineage diversity in multiple sclerosis. *Nature* **573**, 75-82 (2019).
44. H. Lund *et al.*, Competitive repopulation of an empty microglial niche yields functionally distinct subsets of microglia-like cells. *Nature communications* **9**, 4845 (2018).
45. P. S. Thiagarajan *et al.*, Vimentin is an endogenous ligand for the pattern recognition receptor Dectin-1. *Cardiovasc Res* **99**, 494-504 (2013).
46. L. Thomas, L. A. Pasquini, Galectin-3-Mediated Glial Crosstalk Drives Oligodendrocyte Differentiation and (Re)myelination. *Frontiers in cellular neuroscience* **12**, 297 (2018).
47. J. Ma, C. Becker, C. A. Lowell, D. M. Underhill, Dectin-1-triggered recruitment of light chain 3 protein to phagosomes facilitates major histocompatibility complex class II presentation of fungal-derived antigens. *J Biol Chem* **287**, 34149-34156 (2012).
48. J. H. Huang *et al.*, NLRX1 Facilitates Histoplasma capsulatum-Induced LC3-Associated Phagocytosis for Cytokine Production in Macrophages. *Frontiers in Immunology* **9**, 2761 (2018).
49. C. C. da Costa, L. J. van der Laan, C. D. Dijkstra, W. Bruck, The role of the mouse macrophage scavenger receptor in myelin phagocytosis. *Eur J Neurosci* **9**, 2650-2657 (1997).

50. J. B. El Khoury *et al.*, CD36 mediates the innate host response to beta-amyloid. *J Exp Med* **197**, 1657-1666 (2003).
51. G. Manich *et al.*, Role of the CD200-CD200R Axis During Homeostasis and Neuroinflammation. *Neuroscience* **405**, 118-136 (2019).
52. C. M. Wolfe, N. F. Fitz, K. N. Nam, I. Lefterov, R. Koldamova, The Role of APOE and TREM2 in Alzheimer's Disease-Current Understanding and Perspectives. *Int J Mol Sci* **20**, (2018).
53. L. Piccio *et al.*, Blockade of TREM-2 exacerbates experimental autoimmune encephalomyelitis. *Eur J Immunol* **37**, 1290-1301 (2007).
54. H. Lund *et al.*, Fatal demyelinating disease is induced by monocyte-derived macrophages in the absence of TGF-beta signaling. *Nature immunology* **19**, 1-7 (2018).
55. M. R. Kotter, W. W. Li, C. Zhao, R. J. Franklin, Myelin impairs CNS remyelination by inhibiting oligodendrocyte precursor cell differentiation. *The Journal of neuroscience : the official journal of the Society for Neuroscience* **26**, 328-332 (2006).
56. A. Lampron *et al.*, Inefficient clearance of myelin debris by microglia impairs remyelinating processes. *J Exp Med* **212**, 481-495 (2015).
57. F. Guillemin *et al.*, Older Age at Multiple Sclerosis Onset Is an Independent Factor of Poor Prognosis: A Population-Based Cohort Study. *Neuroepidemiology* **48**, 179-187 (2017).
58. M. Yamanaka *et al.*, PPARgamma/RXRalpha-induced and CD36-mediated microglial amyloid-beta phagocytosis results in cognitive improvement in amyloid precursor protein/presenilin 1 mice. *The Journal of neuroscience : the official journal of the Society for Neuroscience* **32**, 17321-17331 (2012).

59. E. Janda, L. Boi, A. R. Carta, Microglial Phagocytosis and Its Regulation: A Therapeutic Target in Parkinson's Disease? *Front Mol Neurosci* **11**, 144 (2018).

60. D. A. Galloway, A. E. M. Phillips, D. R. J. Owen, C. S. Moore, Phagocytosis in the Brain: Homeostasis and Disease. *Frontiers in Immunology* **10**, 790 (2019).

61. C. Settembre *et al.*, TFEB links autophagy to lysosomal biogenesis. *Science (New York, N.Y.)* **332**, 1429-1433 (2011).

62. K. Castillo *et al.*, Trehalose delays the progression of amyotrophic lateral sclerosis by enhancing autophagy in motoneurons. *Autophagy* **9**, 1308-1320 (2013).

63. M. Samie, P. Cresswell, The transcription factor TFEB acts as a molecular switch that regulates exogenous antigen presentation pathways. *Nature immunology* **16**, 729-736 (2015).

64. I. Sergin *et al.*, Exploiting macrophage autophagy-lysosomal biogenesis as a therapy for atherosclerosis. *Nature communications* **8**, 15750 (2017).

65. P. Rusmini *et al.*, Trehalose induces autophagy via lysosomal-mediated TFEB activation in models of motoneuron degeneration. *Autophagy*, 1-21 (2018).

66. P. Lotfi *et al.*, Trehalose reduces retinal degeneration, neuroinflammation and storage burden caused by a lysosomal hydrolase deficiency. *Autophagy* **14**, 1419-1434 (2018).

67. M. Sospedra, R. Martin, Immunology of multiple sclerosis. *Annu Rev Immunol* **23**, 683-747 (2005).

68. R. Yamasaki *et al.*, Differential roles of microglia and monocytes in the inflamed central nervous system. *J Exp Med* **211**, 1533-1549 (2014).

69. A. A. Pimenova, E. Marcora, A. M. Goate, A Tale of Two Genes: Microglial Apoe and Trem2. *Immunity* **47**, 398-400 (2017).

70. Z. Szondy, Z. Sarang, B. Kiss, E. Garabuczi, K. Koroskenyi, Anti-inflammatory Mechanisms Triggered by Apoptotic Cells during Their Clearance. *Frontiers in Immunology* **8**, 909 (2017).

71. B. Spittau, Aging Microglia-Phenotypes, Functions and Implications for Age-Related Neurodegenerative Diseases. *Front Aging Neurosci* **9**, 194 (2017).

72. A. J. Stranks *et al.*, Autophagy Controls Acquisition of Aging Features in Macrophages. *J Innate Immun* **7**, 375-391 (2015).

73. T. D. Evans, S. J. Jeong, X. Zhang, I. Sergin, B. Razani, TFEB and trehalose drive the macrophage autophagy-lysosome system to protect against atherosclerosis. *Autophagy* **14**, 724-726 (2018).

74. M. J. C. Jordao *et al.*, Single-cell profiling identifies myeloid cell subsets with distinct fates during neuroinflammation. *Science* **363**, (2019).

75. L. Chappell-Maor *et al.*, Comparative analysis of CreER transgenic mice for the study of brain macrophages: A case study. *Eur J Immunol*, (2019).

76. S. Amor *et al.*, Identification of epitopes of myelin oligodendrocyte glycoprotein for the induction of experimental allergic encephalomyelitis in SJL and Biozzi AB/H mice. *Journal of immunology (Baltimore, Md. : 1950)* **153**, 4349-4356 (1994).

77. D. Linares, I. Echevarria, P. Mana, Single-step purification and refolding of recombinant mouse and human myelin oligodendrocyte glycoprotein and induction of EAE in mice. *Protein expression and purification* **34**, 249-256 (2004).

78. M. I. Love, W. Huber, S. Anders, Moderated estimation of fold change and dispersion for RNA-seq data with DESeq2. *Genome biology* **15**, 550 (2014).

79. Y. Benjamini, Y. Hochberg, CONTROLLING THE FALSE DISCOVERY RATE - A PRACTICAL AND POWERFUL APPROACH TO MULTIPLE TESTING. *J. R. Stat. Soc. Ser. B-Stat. Methodol.* **57**, 289-300 (1995).

80. W. T. Norton, S. E. Poduslo, Myelination in rat brain: method of myelin isolation. *Journal of neurochemistry* **21**, 749-757 (1973).

81. V. Kaminskyy, A. Abdi, B. Zhivotovsky, A quantitative assay for the monitoring of autophagosome accumulation in different phases of the cell cycle. *Autophagy* **7**, 83-90 (2011).

82. M. Z. Adzemovic, M. Zeitelhofer, S. Hochmeister, S. A. Gustafsson, M. Jagodic, Efficacy of vitamin D in treating multiple sclerosis-like neuroinflammation depends on developmental stage. *Experimental neurology* **249**, 39-48 (2013).

Acknowledgments: The authors would like to thank Dr. Masaaki Komatsu at the Tokyo Metropolitan Institute of Medical Science for providing the *Atg7*$^{fl/fl}$ mice. The authors acknowledge Dr. Klas Blomgren at the University of Gothenburg for providing breeding couples of *Atg7*$^{fl/fl}$ mice. We thank the staff at the animal facility at Karolinska University Hospital and in particular Helen Kungsmark for animal care taking. We also thank Dr. Annika van Vollenhoven for assisting with flow cytometry sorting. We would like to acknowledge support from Science for Life Laboratory, the National Genomics Infrastructure (NGI). **Funding:** This work was supported by grants from the Swedish Research Council, the Swedish Brain Foundation, the Swedish Association for Persons with Neurological Disabilities, the Stockholm County Council (ALF project), AstraZeneca (AstraZeneca-Science for Life Laboratory collaboration), European Union Horizon 2020/European Research Council Consolidator Grant (Epi4MS), the Knut and Alice Wallenbergs Foundation, Margeretha af Ugglas Foundation, Alltid Litt Sterkere, Foundation of Swedish MS research, NEURO Sweden and Karolinska Institutet. **Author contributions:** The study was conceived by RB, AOGC, MTH, TO and MJ. Most experiments were conducted by RB with assistance from AOGC, HL and EN. MTH and RP assisted in EAE characterization. Histopathology and immunofluorescence of CNS were assessed by MZ, EN, SA and MZA. RNA extraction, purification and quality control were performed by RB and SR. RNA-sequencing data preparation and analysis was done by EE and functional annotation analysis by MJ. RB, AOGC, MJ wrote the manuscript with input from other authors. Statistical analysis were done by RB and EE. The project was supervised by AOGC, RAH, TO and MJ. **Competing interests:** The authors report no competing interests. **Data and materials availability:** The RNA-sequencing data has been deposited in the Gene Expression Omnibus (GEO) and the accession number is GSE154920. The mouse strains can be purchased at RikenBRC (B6.Cg-Atg7<tm1Tchi) and Jackson laboratory

(B6.129-Ulk1tm1Thsn/J), (B6.129P2(Cg)-Cx3cr1tm1Litt/J, B6.129P2-Lyz2tm1(cre)Ifo/J, B6.Cg-Tg(Lck-cre)548Jxm/J). All reagents are listed as Technical data with company details and order number (table S5).

894

Figure legends

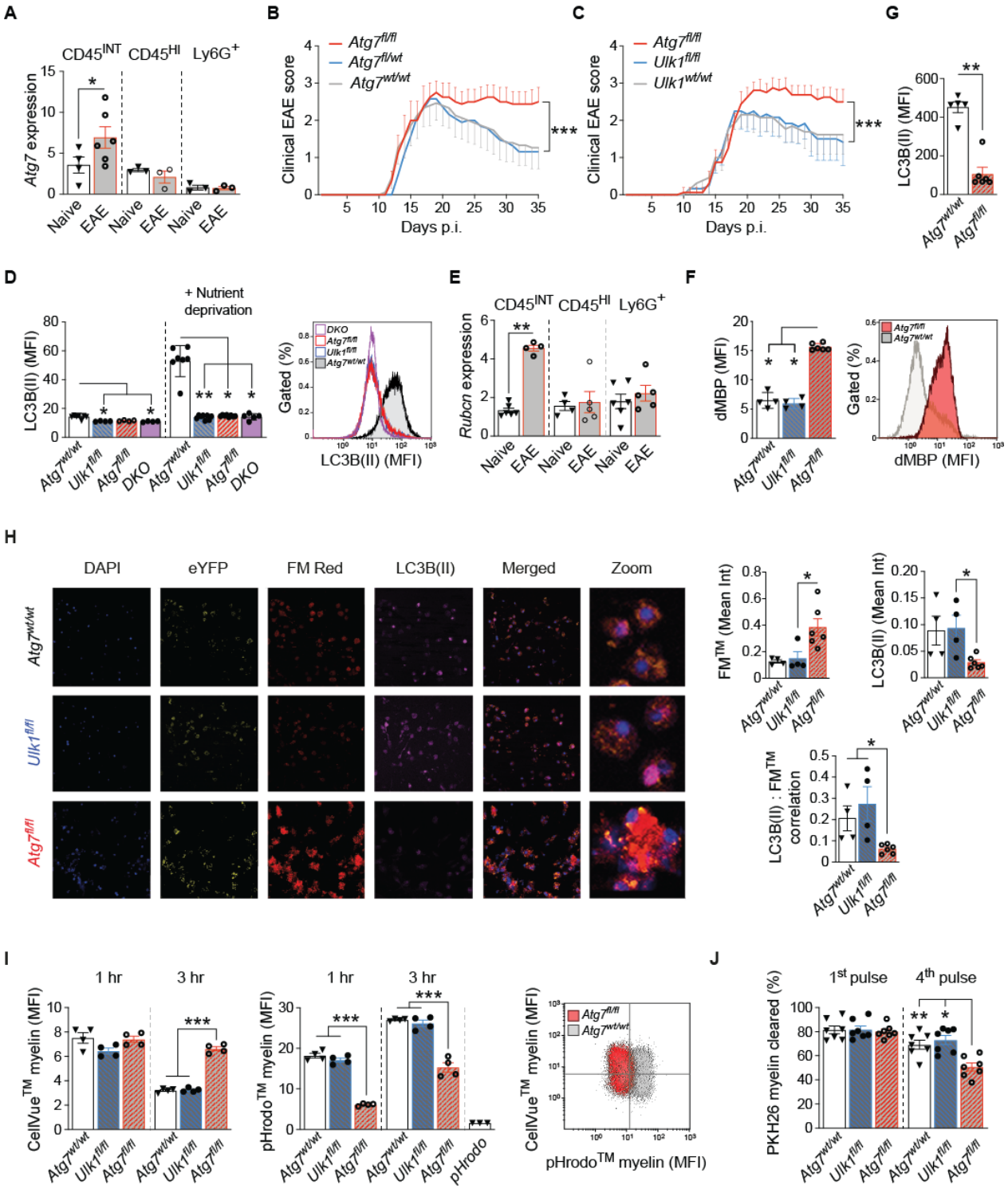

Fig. 1. Recovery from Experimental Autoimmune Encephalomyelitis (EAE) requires microglial autophagy.

(**A**) Relative expression of *Atg7* in microglia ($CD45^{INT}$ naïve; $n = 4$ and EAE; $n = 6$), bone marrow-derived monocytes/macrophages ($CD45^{INT}$ naïve; $n = 3$ and EAE; $n = 3$) and neutrophils ($Ly6G^{+}$ naïve; $n = 3$ and EAE; $n = 3$) from naïve and day 15 EAE animals, detected by qPCR and normalized to the geometric mean of two endogenous control genes, *Gapdh* and *Hprt*. (**B**) Disease course in $Atg7^{wt/wt}$ ($n = 16$), $Atg7^{wt/fl}$ ($n = 20$) and $Atg7^{fl/fl}$ ($n = 19$) mice and (**C**) in $Ulk1^{wt/wt}$ ($n = 13$), $Ulk1^{fl/fl}$ ($n = 12$) and $Atg7^{fl/fl}$ ($n = 16$) mice. Clinical course was compared using one-way ANOVA with Tukey's post-hoc test on Area Under Curve. Error bars indicate confidence intervals. (**D**) Membrane bound LC3B (II) detected by flow cytometry in naïve $Atg7^{wt/wt}$ (untreated; $n = 7$, starved; $n = 7$), $Ulk1^{fl/fl}$ (untreated; $n = 4$, starved; $n = 8$), $Atg7^{fl/fl}$ (untreated; $n = 4$, starved; $n = 8$) and $Atg7^{fl/f}$ $Ulk1^{fl/fl}$ ("double knock-out"- DKO, untreated; $n = 4$, starved; $n = 5$) microglia after starvation *in vitro*. (**E**) Relative expression of *Rubicon* in microglia ($CD45^{INT}$ naïve; $n = 6$ and EAE, $n = 4$), bone marrow-derived monocytes/macrophages ($CD45^{HI}$ naïve; $n = 4$ and EAE; $n = 5$) and neutrophils ($Ly6G^{+}$ naïve; $n = 6$ and EAE; $n = 5$) from naïve and day 15 EAE animals, detected by qPCR and normalized to the geometric mean of two endogenous control genes, *Gapdh* and *B-actin*. (**F**) Phagocytosed myelin debris (dMBP) assessed in microglia from $Atg7^{wt/wt}$, $Ulk1^{fl/fl}$ and $Atg7^{fl/fl}$ mice 21 days p.i. by flow cytometry (all conditions; $n = 5$). (**G**) Membrane bound LC3B (II) detected by flow cytometry after antibody labeling of *ex vivo* microglia 21 days p.i. in $Atg7^{wt/wt}$ ($n = 5$) and $Atg7^{fl/fl}$ ($n = 6$) mice. (**H**) Example images of immunofluorescence and image analysis of Fluoromyelin™ stained myelin (FM Red), LC3B (II) and LC3B (II):Myelin (overlapping pixels) of *ex vivo* microglia 5 days p.i. from $Atg7^{wt/wt}$ ($n = 4$), $Ulk^{fl/fl}$ ($n = 4$) and $Atg7^{fl/fl}$ ($n = 6$) mice. (**I**) *In vitro* pulsing of microglia 5 days p.i. with CellVue™- and

pHrodo^{TM}-stained myelin, assessed by flow cytometry (all conditions: n = 4 except "pHrodo" n = 3). (**J**) *In vitro* clearance of PKH26-stained myelin from medium by microglia 5 days p.i. from *Atg7*$^{wt/wt}$ (n = 7) and *Atg7*$^{fl/fl}$ (n = 7) mice. Statistics: (**A**, **E** and **G**) Mann-Whitney U-test, (**D**, **F**, **H** and **J**) Kruskal–Wallis test followed by Dunn's post-hoc test, (**I**) ANOVA followed by Dunnet's post-hoc test (*** $p < 0.001$, ** $p < 0.01$, * $p < 0.05$). Error bars indicate SEM. Experiments (**A** to **D** and **E**, **H**) were performed twice and (**B**, **C**, **F**, **G**, **I**, **J**) three times.

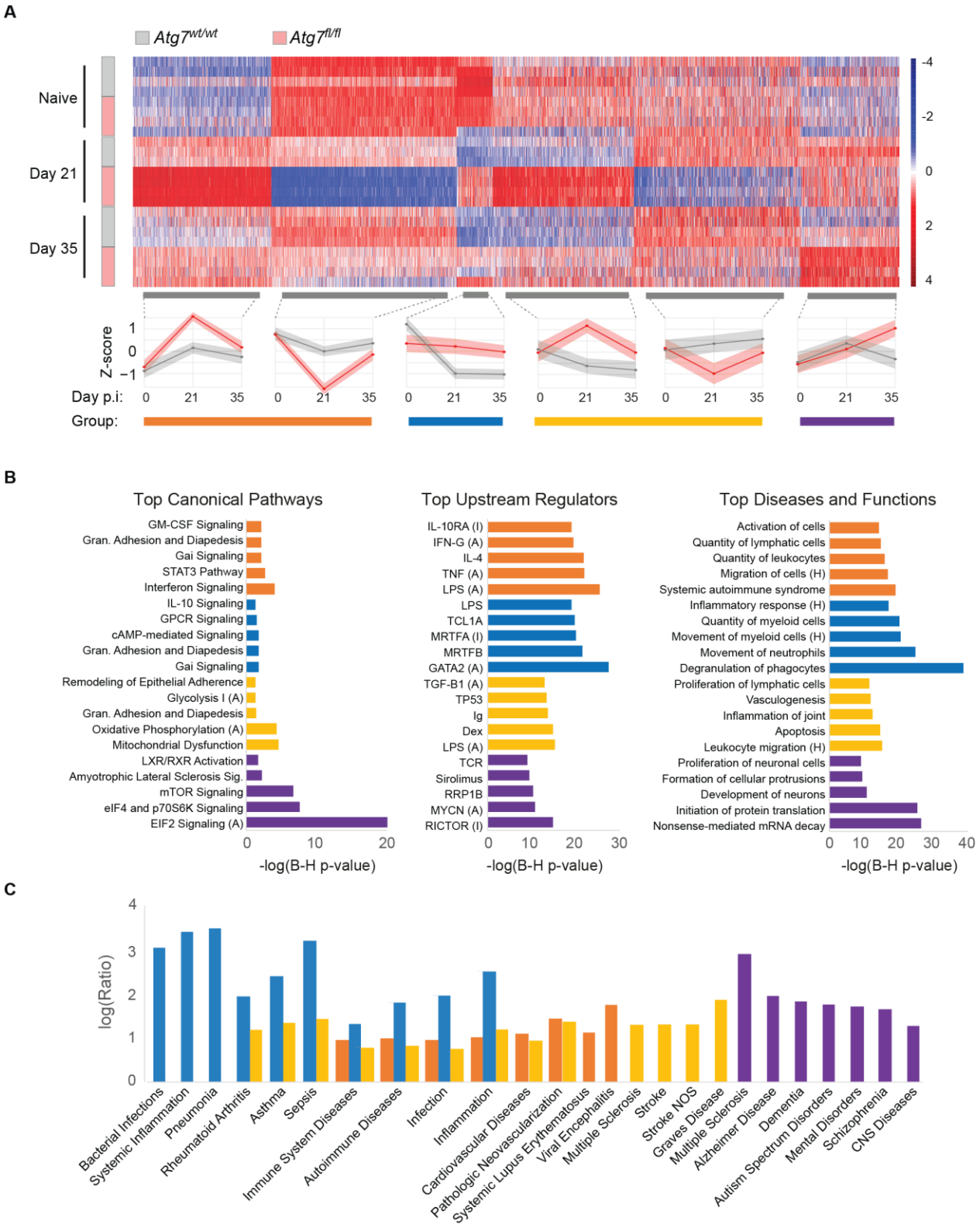
A
Atg7wt/wt
Atg7fl/fl
Naive
Day 21
Day 35
-4
-2
0
2
4
Z-score
1
0
−1
Day p.i:
0
21
35
Group:
B
Top Canonical Pathways
GM-CSF Signaling
Gran. Adhesion and Diapedesis
Gai Signaling
STAT3 Pathway
Interferon Signaling
IL-10 Signaling
GPCR Signaling
cAMP-mediated Signaling
Gran. Adhesion and Diapedesis
Gai Signaling
Remodeling of Epithelial Adherence
Glycolysis I (A)
Gran. Adhesion and Diapedesis
Oxidative Phosphorylation (A)
Mitochondrial Dysfunction
LXR/RXR Activation
Amyotrophic Lateral Sclerosis Sig.
mTOR Signaling
eIF4 and p70S6K Signaling
EIF2 Signaling (A)
0
10
20
-log(B-H p-value)
Top Upstream Regulators
IL-10RA (I)
IFN-G (A)
IL-4
TNF (A)
LPS (A)
LPS
TCL1A
MRTFA (I)
MRTFB
GATA2 (A)
TGF-B1 (A)
TP53
Ig
Dex
LPS (A)
TCR
Sirolimus
RRP1B
MYCN (A)
RICTOR (I)
0
10
20
30
-log(B-H p-value)
Top Diseases and Functions
Activation of cells
Quantity of lymphatic cells
Quantity of leukocytes
Migration of cells (H)
Systemic autoimmune syndrome
Inflammatory response (H)
Quantity of myeloid cells
Movement of myeloid cells (H)
Movement of neutrophils
Degranulation of phagocytes
Proliferation of lymphatic cells
Vasculogenesis
Inflammation of joint
Apoptosis
Leukocyte migration (H)
Proliferation of neuronal cells
Formation of cellular protrusions
Development of neurons
Initiation of protein translation
Nonsense-mediated mRNA decay
0
10
20
30
40
-log(B-H p-value)
C
log(Ratio)
0
1
2
3
4
Bacterial Infections
Systemic Inflammation
Pneumonia
Rheumatoid Arthritis
Asthma
Sepsis
Immune System Diseases
Autoimmune Diseases
Infection
Inflammation
Cardiovascular Diseases
Pathologic Neovascularization
Systemic Lupus Erythematosus
Viral Encephalitis
Multiple Sclerosis
Stroke
Stroke NOS
Graves Disease
Multiple Sclerosis
Alzheimer Disease
Dementia
Autism Spectrum Disorders
Mental Disorders
Schizophrenia
CNS Diseases

927

Fig. 2. *Atg7* deficiency induces pronounced and sustained alterations in microglial transcriptome during Experimental Autoimmune Encephalomyelitis (EAE).

Transcriptome analysis was performed using RNA-sequencing of microglia sorted from the following groups of mice: naive $Atg7^{fl/fl}$ (n = 4) and $Atg7^{wt/wt}$ (n = 3), day 21 p.i. $Atg7^{fl/fl}$ (n = 4, average score 3) and $Atg7^{wt/wt}$ (n = 3, average score 3) and day 35 p.i. $Atg7^{fl/fl}$ (n = 3, average score 1.5) and $Atg7^{wt/wt}$ (n = 4, average score 2.5) (table S1). (**A**) Heat map depicting gene clusters associated with genotype and EAE disease stage based on transcripts that displayed a p-value < 0.01 and fold-change > 1.5. The scale represents Z-score transformed expression values (with red and blue indicating upregulated and downregulated genes, respectively, compared to the mean value of a gene from all samples). These gene clusters were further grouped according to their pattern of expression into the four groups that were analyzed using Ingenuity pathway analysis™ (IPA) to annotate significance: (**B**) Canonical pathways, Upstream regulators, and Diseases and Functions (Benjamini-Hochberg adjusted p-value < 0.05) and (**C**) Over-representation analysis (ORA) for Diseases using the GLAD4U database (FDR < 0.05). Details regarding the differential expression analysis are presented in table S1 and a full list of significant functional annotations is provided in table S2. (A), (I) and (H) indicate activated, inhibited and high, respectively.

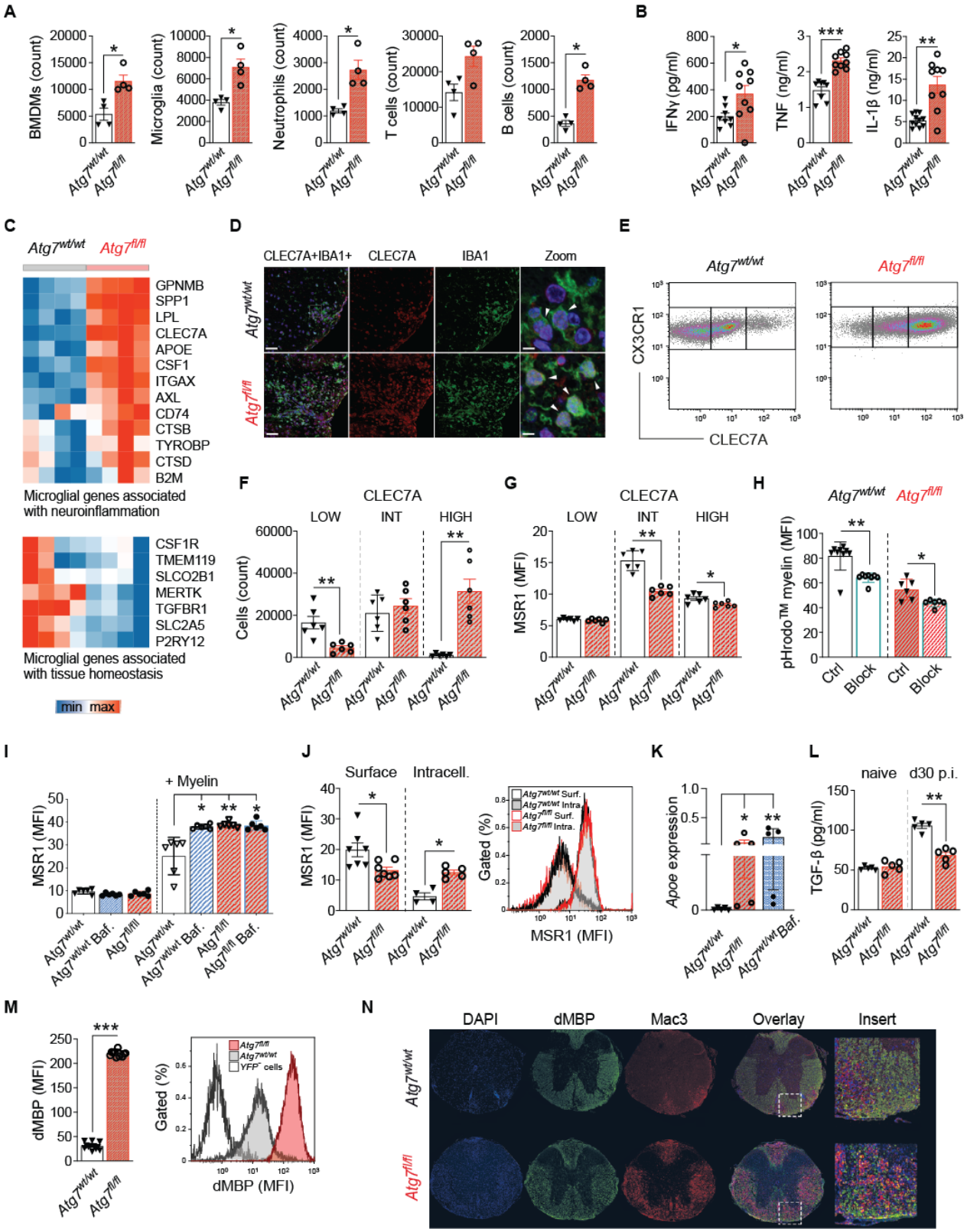
A
BMDMs (count)
Microglia (count)
Neutrophils (count)
T cells (count)
B cells (count)
Atg7wt/wt
Atg7fl/fl
B
IFNγ (pg/ml)
TNF (ng/ml)
IL-1β (ng/ml)
C
Atg7wt/wt
Atg7fl/fl
GPNMB
SPP1
LPL
CLEC7A
APOE
CSF1
ITGAX
AXL
CD74
CTSB
TYROBP
CTSD
B2M
Microglial genes associated with neuroinflammation
CSF1R
TMEM119
SLCO2B1
MERTK
TGFBR1
SLC2A5
P2RY12
Microglial genes associated with tissue homeostasis
min
max
D
CLEC7A+IBA1+
CLEC7A
IBA1
Zoom
E
CX3CR1
CLEC7A
F
CLEC7A
LOW
INT
HIGH
Cells (count)
G
MSR1 (MFI)
H
pHrodo™ myelin (MFI)
Ctrl
Block
I
+ Myelin
Atg7wt/wt Baf.
Atg7fl/fl Baf.
J
Surface
Intracell.
Gated (%)
K
Apoe expression
L
naive
d30 p.i.
TGF-β (pg/ml)
M
dMBP (MFI)
YFP- cells
N
DAPI
dMBP
Mac3
Overlay
Insert

944

945

Fig. 3. *Atg7*-deficient microglia have impaired myelin degradation and scavenger receptor recirculation associated to a pathogenic phenotype and increased inflammation in Experimental Autoimmune Encephalomyelitis (EAE).

(**A**) Spinal cord microglia and infiltrating immune cell counts from $Atg7^{wt/wt}$ (n = 4) and $Atg7^{fl/fl}$ (n = 4) mice at day 21 p.i. analyzed by flow cytometry. (**B**) ELISA of supernatants from microglia sorted 21 days p.i. and incubated for 24h *in vitro*; $Atg7^{wt/wt}$ (n = 8) and $Atg7^{fl/fl}$ (n = 9). (**C**) Transcriptome of microglia sorted from $Atg7^{wt/wt}$ (n = 4) and $Atg7^{fl/fl}$ (n = 4) mice 35 days p.i. analyzed by RNA-sequencing and compared to microglia gene sets associated with disease and tissue homeostasis. (**D**) Representative images of immunofluorescence of CLEC7A and IBA1-expressing microglia at day 32-37 p.i. in spinal cord from $Atg7^{wt/wt}$ and $Atg7^{fl/fl}$ mice. DAPI defines nuclei. Size bars correspond to 500µm and 50µm in the left and right panels, respectively. (**E** and **F**) Flow cytometry analysis of CLEC7A-expressing subpopulations in $Atg7^{wt/wt}$ (n = 6) and $Atg7^{fl/fl}$ (n = 6) microglia at day 35 p.i. (**G**) Flow cytometry analysis of the density of surface MSR1 staining in microglia from $Atg7^{wt/wt}$ (n = 6) and $Atg7^{fl/fl}$ (n = 6) mice in different subpopulations defined by levels of CLEC7A expression as shown in (**E** and **F)**. (**H**) Uptake of labeled myelin by sorted $Atg7^{wt/wt}$ (control; n = 9, block; n = 8) and $Atg7^{fl/fl}$ (control; n = 6, block; n = 6) microglia after blocking of MSR1. (**I**) Flow cytometry quantification of intracellular MSR1 from naïve $Atg7^{wt/wt}$ and $Atg7^{fl/fl}$ microglia exposed to myelin 12h *in vitro* w/wo 6h Bafilomycin A1 treatment. All conditions; n = 6. (**J**) Surface and intracellular MSR1 detection by flow cytometry in $Atg7^{wt/wt}$ (surface; n = 7, intracellular; n = 4) and $Atg7^{fl/fl}$ (surface; n = 7, intracellular; n = 5) microglia day 5 p.i. (**K**) Expression of *Apoe* in $Atg7^{wt/wt}$ (n = 4), $Atg7^{fl/fl}$ (n = 5) and Bafilomycin A1 treated $Atg7^{wt/wt}$ (n = 5) microglia exposed to myelin for 7 days *in vitro*. (**L**) ELISA of TGF-β1 secretion from microglia from *naïve* and day 35 p.i. mice ($Atg7^{wt/wt}$; n = 5, $Ulk^{fl/fl}$; n = 5 and $Atg7^{fl/fl}$;

969 $n = 5$) after 24h *in vitro* culture. (**M**) Intracellular myelin debris (dMBP) assessed in microglia from
970 $Atg7^{wt/wt}$ ($n = 12$) and $Atg7^{fl/fl}$ ($n = 12$) mice 35 days p.i. by flow cytometry. (**N**) Representative
971 images of immunofluorescence of tissue deposits of myelin debris (dMBP) and density of $Mac3^{+}$
972 macrophages at 37 p.i. in spinal cord from $Atg7^{wt/wt}$ and $Atg7^{fl/fl}$ mice. DAPI defines nuclei.
973 Statistics: (**A**, **B**, **F** to **H**, **J**, **L**, **M**) Mann-Whitney U-test, (**I** and **K**) Kruskal–Wallis test followed
974 by Dunn's post-hoc test (*** $p < 0.001$, ** $p < 0.01$, * $p < 0.05$). Error bars indicate SEM.
975 Experiment (**N**) is representative of three independent experiments. Experiments (**B**, **H** to **M**) were
976 performed twice and (**A**, **F**, **G**) three times.

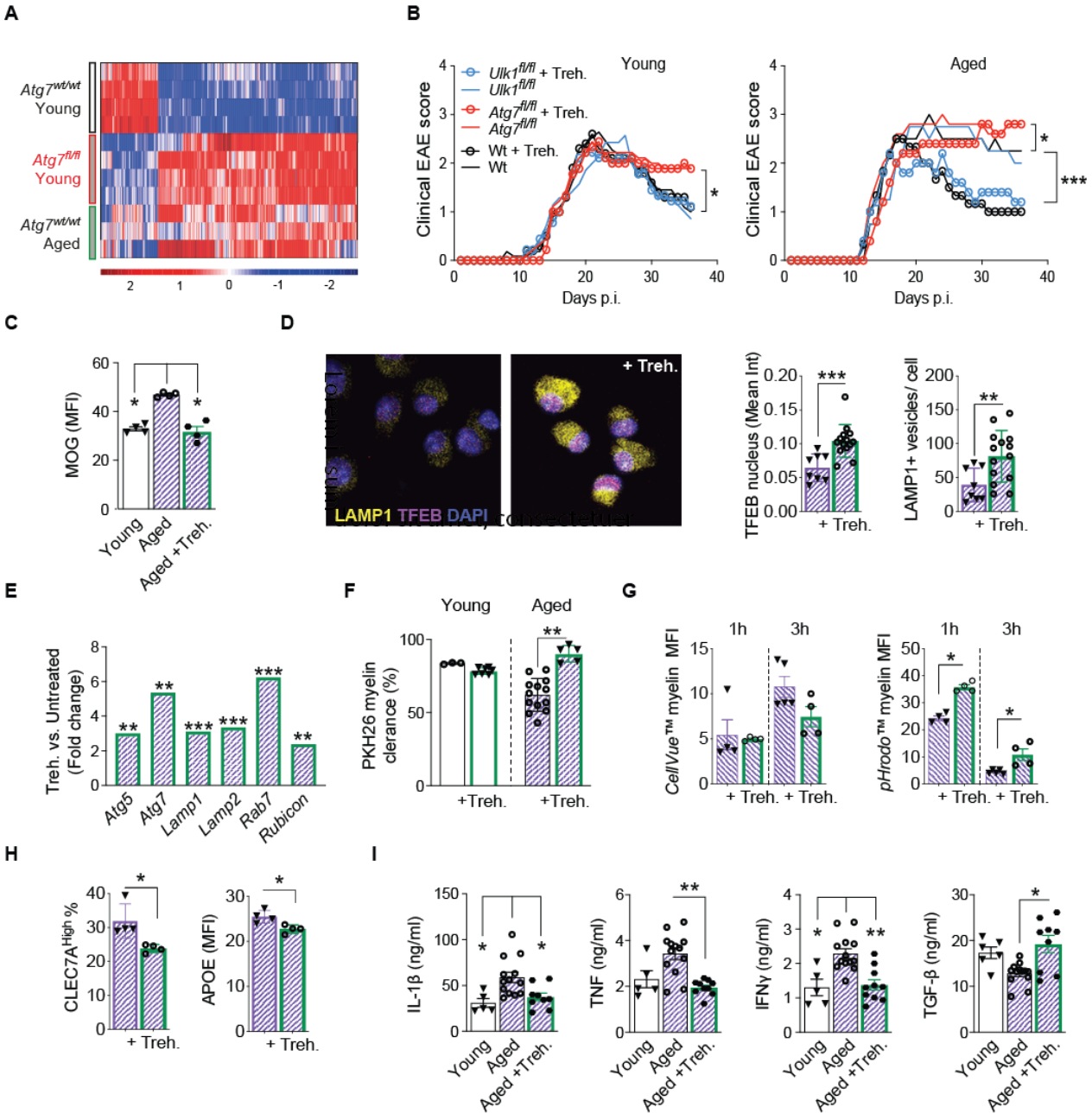

977

978 **Fig. 4. Trehalose treatment boosts myelin clearance and ameliorates Experimental**

979 **Autoimmune Encephalomyelitis (EAE) in aged mice.**

980 (**A**) Transcriptome heat map of microglia sorted from naïve aged (> 80 weeks) wild type mice (*n*

981 = 3, average score 2.5) and *Atg7*$^{wt/wt}$ (*n* = 4, average EAE score 1.5) and *Atg7*$^{fl/fl}$ (*n* = 4, average

982 EAE score 2.5) mice 35 days p.i. analyzed by RNA-sequencing (table S4). The scale represents Z-

score transformed expression values (with red and blue indicating upregulated and downregulated genes, respectively, compared to the mean value of a gene from all samples). (**B**) Clinical course of EAE and full recovery rate in young (12-22 weeks old) *Atg7*$^{wt/wt}$ (control; n = 11, treated; n = 11), *Ulk1*$^{fl/fl}$ (control; n = 7, treated; n = 9) and *Atg7*$^{fl/fl}$ (control; n = 9, treated; n = 9) mice (left) and aged *Atg7*$^{wt/wt}$ (control; n = 4, treated; n = 6), *Ulk1*$^{fl/fl}$ (control; n = 4, treated; n = 5) and *Atg7*$^{fl/fl}$ (control; n = 5, treated; n = 5) mice (right). Mice were fed with Trehalose in water or water as control. Clinical course was compared using one-way ANOVA with Tukey's post-hoc test on Area Under Curve. (**C**) Flow cytometry quantification of intracellular myelin debris in microglia from young (n = 3), aged (n = 4) and Trehalose-treated aged (n = 4) mice at day 21 p.i. (**D**) Immunofluorescence image and quantification showing TFEB translocation from cytosol to nucleus upon 48h *in vitro* Trehalose-treated (n = 14) and untreated (n = 8) microglia from aged mice at day 5 p.i. LAMP1 detects lysosomal structures. Data pooled from two experiments. (**E**) Expression of selected key autophagosome, lysosome and phagosome vesicle biogenesis genes in microglia of aged mice (n = 9) after 48h of *ex vivo* Trehalose treatment as fold change of untreated control. (**F**) *In vitro* myelin clearance assay of microglia sorted 5 days p.i. from young (n = 3), aged (n = 13) and Trehalose-treated young (n = 7) and aged (n = 5) mice pulsed 4 times with PKH26-labeled myelin. (**G**) *In vitro* pulsing of microglia 5 days p.i. with CellVue^{TM}- and pHrodo^{TM}-stained myelin, assessed by flow cytometry (all conditions: n = 4 except aged 3h; n = 5). (**H**) CLEC7A and APOE detected by Flow cytometry on ex vivo day 21 EAE microglia from Aged (n = 4) w/wo Trehalose treatment (n = 4). (**I**) ELISA of cytokine production by CD11b^{+} cells isolated from the CNS of young (n = 5), aged (n = 13) and Trehalose-treated aged (n = 10) mice at day 21 p.i. cultured *ex vivo* for 24h. Statistics: (**D, F** to **H**) Mann-Whitney U-test, (**C** and **I**) Kruskal–Wallis test

followed by Dunn's post-hoc test (*** $p < 0.001$, ** $p < 0.01$, * $p < 0.05$). Error bars indicate SEM. Experiments (**B** to **D** and **F** to **I**) were performed twice.

Supplementary Figure 1

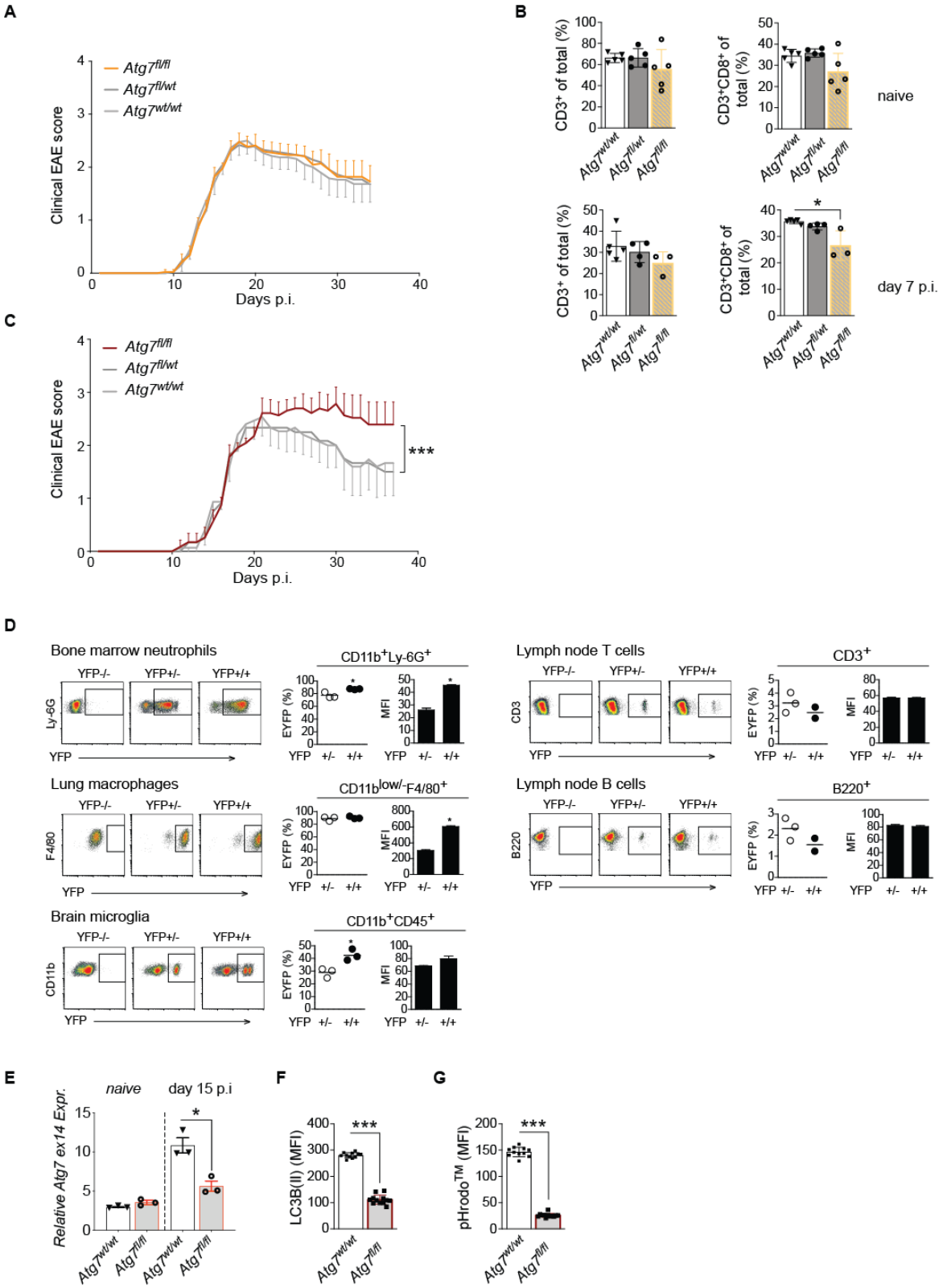

Fig. S1. Recovery from Experimental Autoimmune Encephalomyelitis (EAE) requires functional autophagy in the myeloid but not in the T cell compartment.

(**A**) Myelin Oligodendrocyte Glycoprotein (MOG)-induced EAE in $Atg7^{fl/fl}Lck^{Cre}$ (n = 44), $Atg7^{fl/wt}Lck^{Cre}$ (n = 43) and $Atg7^{wt/wt}Lck^{Cre}$ (n = 38) mice (three pooled experiments). (**B**) Frequencies of cells from inguinal lymph nodes in $Atg7^{fl/fl}Lck^{Cre}$ (n = 3-5), $Atg7^{fl/wt}Lck^{Cre}$ (n = 4-5), and $Atg7^{wt/wt}Lck^{Cre}$ (n = 5) mice as detected by flow cytometry. (**C**) MOG-induced EAE in $Atg7^{fl/fl}Lyz2^{Cre}$ (n = 15), $Atg7^{fl/wt}Lyz2^{Cre}$ (n = 10) and $Atg7^{wt/wt}Lyz2^{Cre}$ (n = 23) mice. (**D**) LysM (*Lyz2*) expression was screened using a reporter system (*Lyz2*-Cre x Rosa26-STOP-YFP). Cells from different tissues were extracted, stained with fluorescently labeled antibodies, acquired by flow cytometry and analyzed by gating into different subsets according to the strategy defined above in the graphs. YFP positivity is shown for control, heterozygous or homozygous animals in representative plots, as well as frequencies of positive cells (shown as percent of each given population) and mean fluorescence intensity (MFI) for YFP expression. Bone marrow neutrophils and lung macrophages show near complete labelling, as expected. In microglia, 30-40% of cells in the naïve state exhibit *Lyz2* expression, while T and B cells show minimal targeting. (**E**) mRNA expression of *Atg7* loxP-flanked exon 14 normalized to *Gapdh* and *β-actin* in microglia from $Atg7^{fl/fl}Lyz2^{Cre}$ (*naïve*; n = 3, day 15 p.i.; n = 3) and $Atg7^{wt/wt}\ Lyz2^{Cre}$ controls (*naïve*; n = 3, day 15 p.i.; n = 3). (**F**) Membrane-bound LC3B (II) and (**G**) intracellular pHrodo™-labeled myelin detected in *ex vivo* day 30 p.i. microglia from $Atg7^{fl/fl}Lyz2^{Cre}$ (n = 12) and $Atg7^{wt/wt}\ Lyz2^{Cre}$ (n = 11) mice by flow cytometry after 48h of myelin and LPS exposure *in vitro*. Statistics: (**A** and **C**) One-way ANOVA with Tukey's post-hoc test on Area Under Curve. Error bars indicate confidence interval; (**B**) Kruskal–Wallis test followed by Dunn's post-hoc test, (**D, F** to **G**) Mann-Whitney U-test, (**E**) Unpaired T-test (*** $p < 0.001$, ** $p < 0.01$, * $p < 0.05$). Error bars indicate SEM. Experiments (**A** to **C**) were performed three times and (**E** to **G**) were performed twice.

Supplementary Figure 2

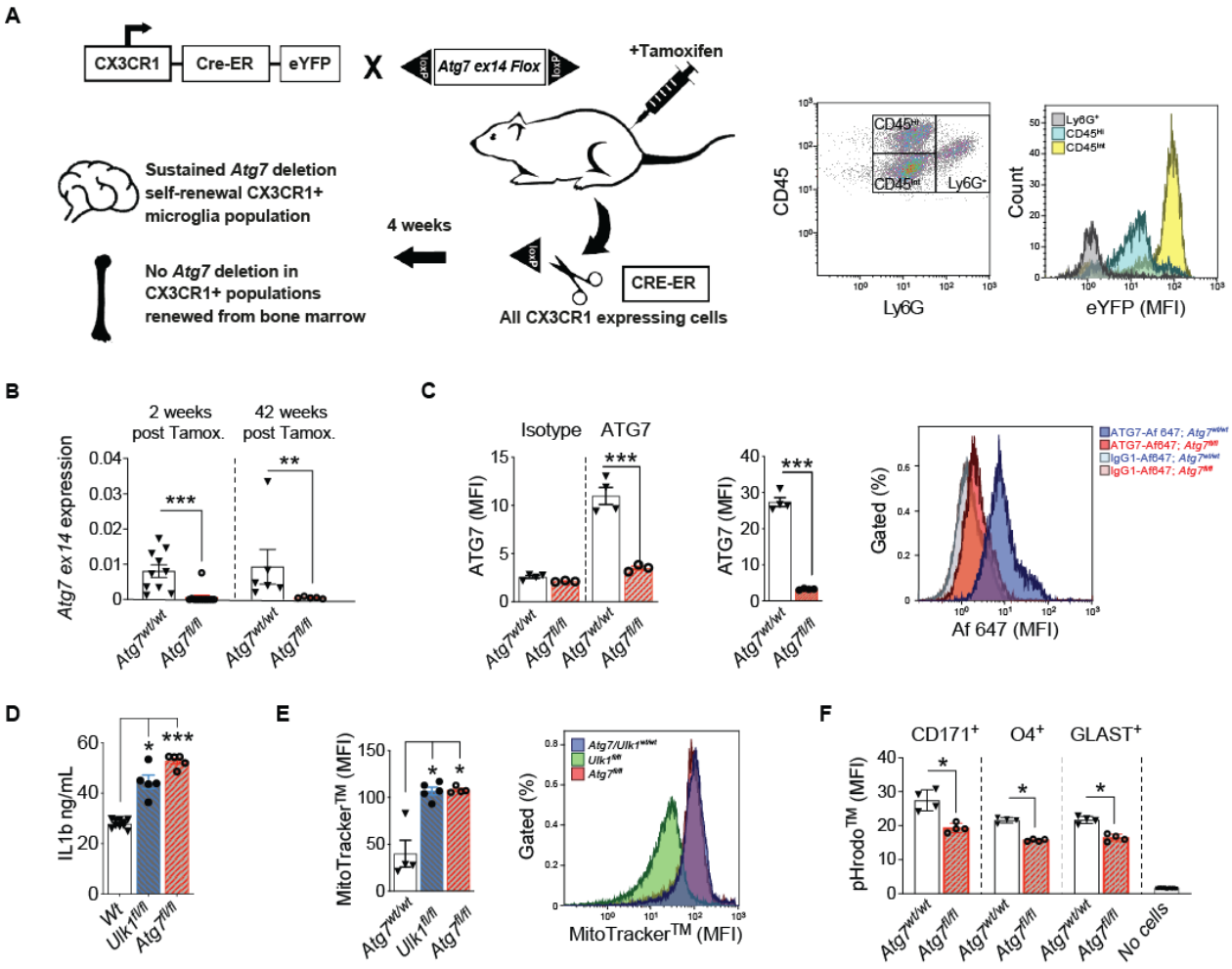

Fig. S2. *Atg7* and *Ulk1* deficiency in microglia impact non-canonical and canonical autophagy, respectively.

(**A**) Scheme over the Tamoxifen inducible *Cx3cr1*^{CreERT2} gene deletion model. *Cx3cr1*^{CreERT2} is co-expressed with fluorescent eYFP. Expression of eYFP in infiltrating CD11b^{+}CD45^{hi} (monocytes), CD11b^{+}CD45$^{hi/int}$ Ly6G^{+} (neutrophils) and CD11b^{int}CD45^{int} (microglia) is shown in the flow cytometry panels to the right. (**B**) mRNA expression of loxP-flanked *Atg7* exon 14 normalized to *Gapdh* and *Hprt* in microglia from *Atg7*$^{fl/fl}$*Cx3cr1*^{CreERT2} (2 weeks; *n* =12, 42 weeks; *n* = 5) and *Atg7*$^{wt/wt}$*Cx3cr1*^{CreERT2} (2 weeks; *n* =10, 42 weeks; *n* = 6) mice. (**C**) Flow cytometry detection of ATG7 in microglia after *in vitro* (left) and *in vivo* (right) Tamoxifen-induced *Atg7* deletion in *Atg7*$^{fl/fl}$*Cx3cr1*^{CreERT2} (*n* = 3) and *Atg7*$^{wt/wt}$ *Cx3cr1*^{CreERT2} (*n* = 4) mice. (**D**) IL-1β secretion by day 15 p.i. microglia from *Atg7*$^{wt/wt}$ *Cx3cr1*^{CreERT2} (*n* = 10), *Ulk1*$^{fl/fl}$*Cx3cr1*^{CreERT2} (*n* = 5) and *Atg7*$^{fl/fl}$

Cx3cr1^{CreERT2} (n = 5) mice. (**E**) Mitochondrial membrane potential detected in *in vitro* LPS treated and nutrient deprived *Atg7*$^{wt/wt}$ *Cx3cr1*^{CreERT2} (n = 4), *Ulk1*$^{fl/fl}$*Cx3cr1*^{CreERT2} (n = 5) and *Atg7*$^{fl/fl}$ *Cx3cr1*^{CreERT2} (n = 4) microglia. (**F**) Phagocytosis of pHrodo^{TM}-labeled apoptotic cells by *Atg7*$^{fl/fl}$-*Cx3cr1*^{CreERT2} (n = 4) and *Atg7*$^{wt/wt}$ *Cx3cr1*^{CreERT2} (n = 4) microglia quantified by flow cytometry. Statistics: (**B** and **F**) Mann-Whitney U-test, (**C**) Unpaired T-test, (**D** and **E**) Kruskal–Wallis test followed by Dunn's post-hoc test (*** $p < 0.001$, ** $p < 0.01$, * $p < 0.05$). Error bars indicate SEM. Experiments (**D** and **E**) were performed twice.

Supplementary Figure 3

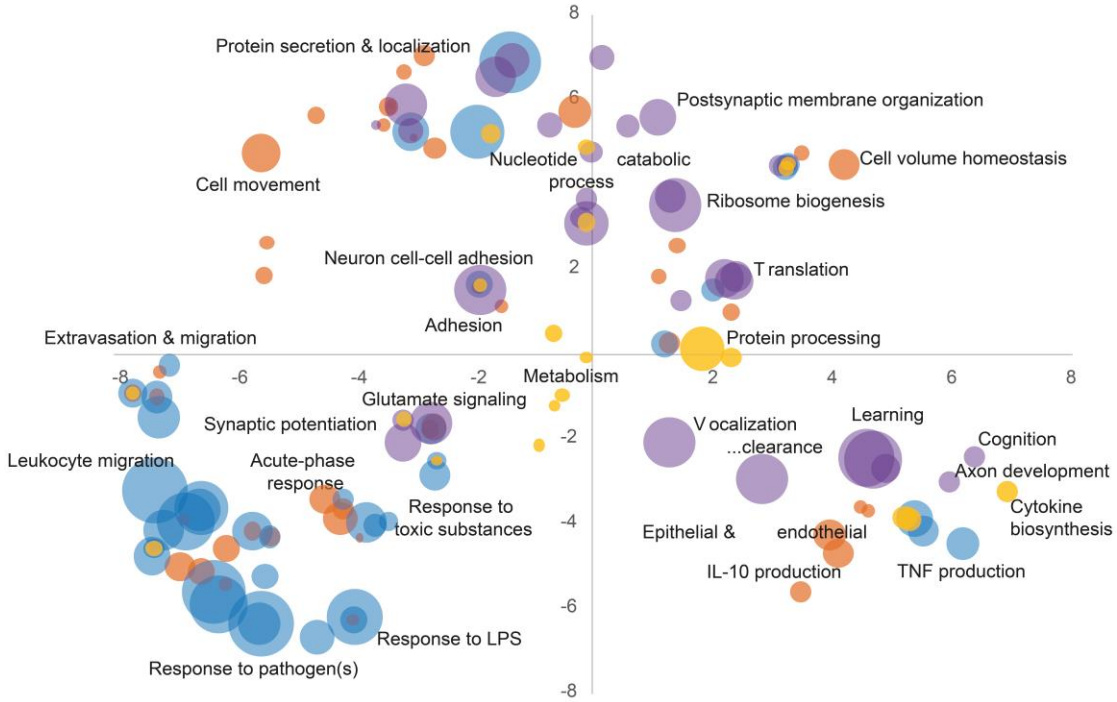

Fig. S3. *Atg7* deficiency induces alterations in microglial transcriptome during Experimental Autoimmune Encephalomyelitis (EAE).

Transcriptomic analysis was performed using RNA-sequencing of microglia sorted from naive *Atg7*$^{fl/fl}$ *Cx3cr1*^{CreERT2} (n = 4) and *Atg7*$^{wt/wt}$ *Cx3cr1*^{CreERT2} (n = 3) mice, at 21 days p.i. from *Atg7*$^{fl/fl}$ *Cx3cr1*^{CreERT2} (n = 4, average score 3) and *Atg7*$^{wt/wt}$ *Cx3cr1*^{CreERT2} (n = 3, average score 3) mice, and at day 35 p.i. from *Atg7*$^{fl/fl}$ *Cx3cr1*^{CreERT2} (n = 3, average score 1.5) and *Atg7*$^{wt/wt}$ *Cx3cr1*^{CreERT2} (n = 4, average score 2.5) mice. REViGO visualization of Gene Ontology terms for Biological Processes for four different patterns of changes: orange - represents changes, considerably more pronounced in *Atg7*$^{fl/fl}$ *Cx3cr1*^{CreERT2} microglia that occurred early in disease (day 21 p.i.) and returned to levels in the naïve state by day 35 p.i. (Fig. 2A); blue - represents genes that remained downregulated during disease with *Atg7*$^{fl/fl}$ *Cx3cr1*^{CreERT2} microglia showing modest changes (Fig. 2A); yellow - had similar pattern to orange in wild type but *Atg7*$^{fl/fl}$ *Cx3cr1*^{CreERT2} microglia demonstrated the opposite pattern (Fig. 2A); purple - represents genes that gradually increased their expression during disease progression specifically in *Atg7*$^{fl/fl}$ *Cx3cr1*^{CreERT2} microglia (Fig. 2A). Details regarding the differential expression analysis are presented in table S1 and a full list of significant functional annotations is provided in table S2.

1071

Supplementary Figure 4

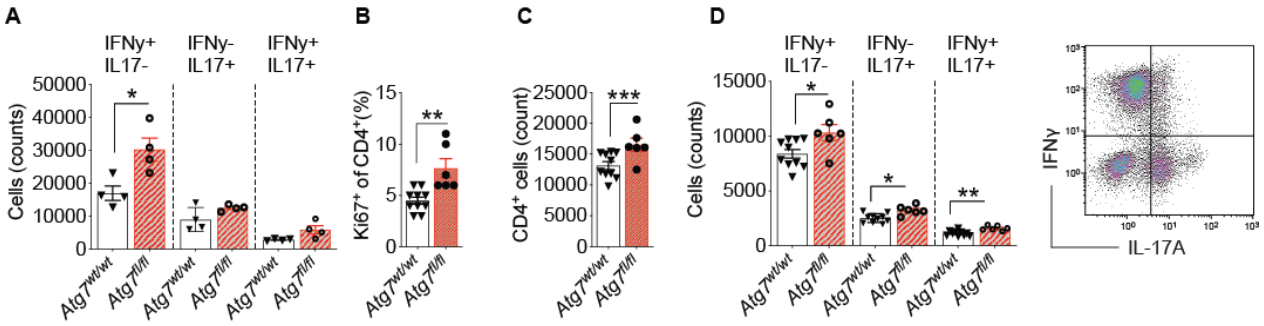

Fig. S4. *Atg7* deficiency in microglia increases T cell proliferation and polarization to an inflammatory phenotype.

(**A**) Cytokine secretion profile of $CD3^+$ T cell infiltrating the spinal cord of mice day 21 p.i. Data shows cell counts assessed by flow cytometry in $Atg7^{wt/wt}Cx3cr1^{CreERT2}$ (n = 4) and $Atg7^{fl/fl}Cx3cr1^{CreERT2}$ (n = 4) mice. (**B**) Flow cytometry detection of $Ki67^+$ expression in T cells sorted from mouse central nervous system day 21 p.i. and co-cultured *in vitro* with $Atg7^{wt/wt}Cx3cr1^{CreERT2}$ (n = 10) and $Atg7^{fl/fl}Cx3cr1^{CreERT2}$ (n = 6) microglia for 36h. (**C**) Total counts of $CD4^+$ T cells after co-culture with $Atg7^{wt/wt}Cx3cr1^{CreERT2}$ and $Atg7^{fl/l}Cx3cr1^{CreERT2}$ microglia as described in (**B**). (**D**) Cytokine secretion profile from $CD4^+$ T cells in the setup described in (**B**), as assessed by flow cytometry. Statistics: Mann-Whitney U-test for all comparisons (***p < 0.001, **p < 0.01, *p < 0.05). Error bars indicate SEM. Experiments (**A** to **D**) were performed twice.

Supplementary Figure 5

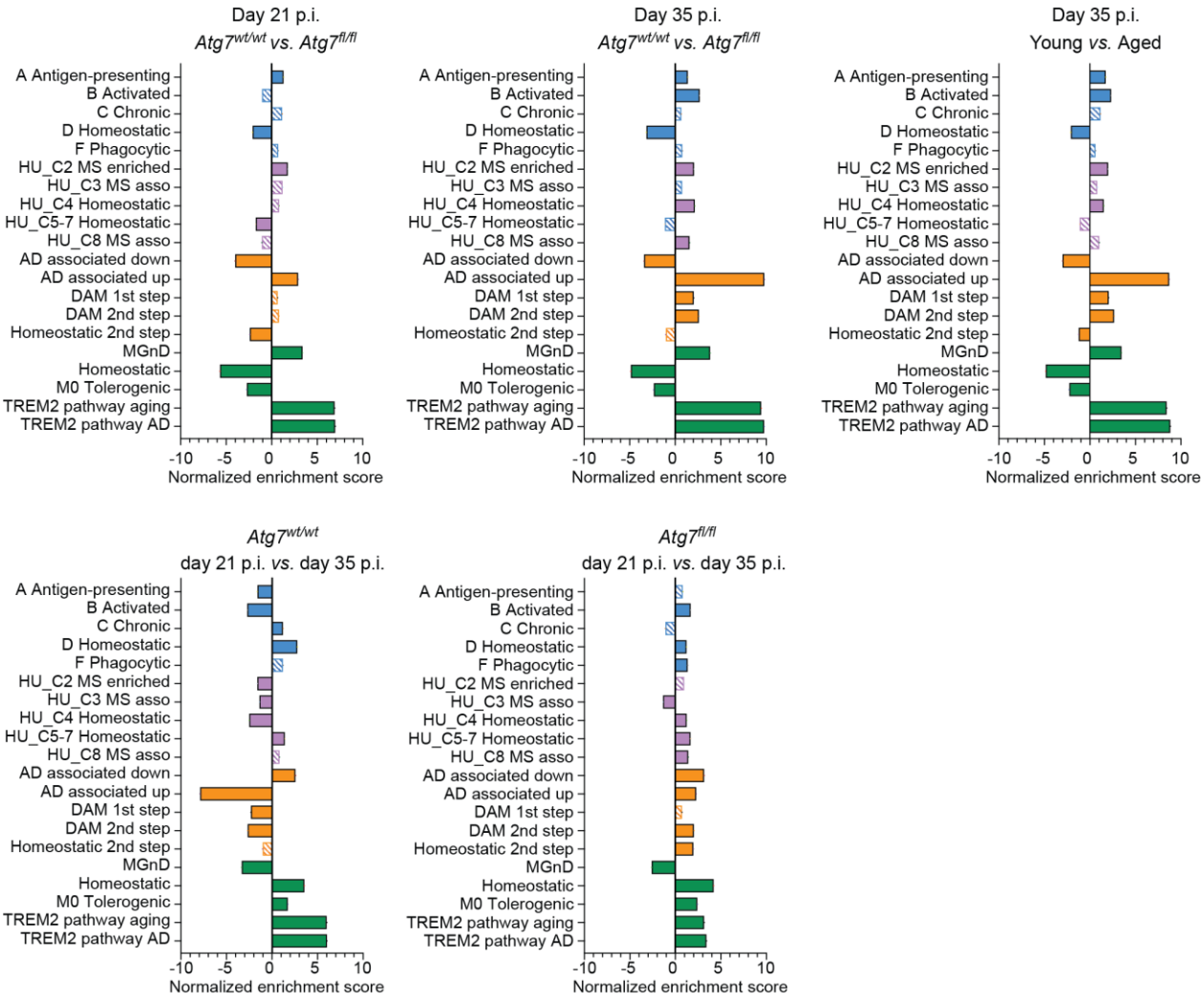

"Neuronal vulnerability and multilineage diversity in multiple sclerosis". Nature. 2019 Sep;573(7772):75-82. (PMID: 31316211).
"Spatial and temporal heterogeneity of mouse and human microglia at single-cell resolution". Nature. 2019 Feb;566(7744):388-392. (PMID: 30760929).
"A Unique Microglia Type Associated with Restricting Development of Alzheimer's Disease". Cell. 2017 Jun 15;169(7):1276-1290.e17. (PMID: 28602351).
"The TREM2-APOE Pathway Drives the Transcriptional Phenotype of Dysfunctional Microglia in Neurodegenerative Diseases". Immunity. 2017 Sep 19; 47(3):566-581.e9. (PMID:28930663).

Fig. S5. Gene-set enrichment analysis.

Gene-set enrichment analysis of transcriptomes from sorted microglia at 21 days p.i. *Atg7*$^{fl/fl}$*Cx3cr1*^{CreERT2} (n = 4, average EAE score 3) and *Atg7*$^{wt/wt}$*Cx3cr1*^{CreERT2} (n = 3, average EAE score 3) and at day 35 p.i. *Atg7*$^{fl/fl}$*Cx3cr1*^{CreERT2} (n = 3, average EAE score 1.5), *Atg7*$^{wt/wt}$*Cx3cr1*^{CreERT2} (n = 4, average EAE score 2.5) and aged *Atg7*$^{wt/wt}$*Cx3cr1*^{CreERT2} (n = 3, average EAE score 2.5). Filled bars indicate significant enrichment (FDR q-value < 0.25) Microglial reference gene sets from human and mouse models of central nervous system disease

were extracted from publications as listed in the figure. Analysis was performed using whole gene signatures and the most significant genes defined by publications. All gene sets and references can be found in table S3. Detailed information on transcriptome analysis can be found in table S1 and S3.

Supplementary Figure 6

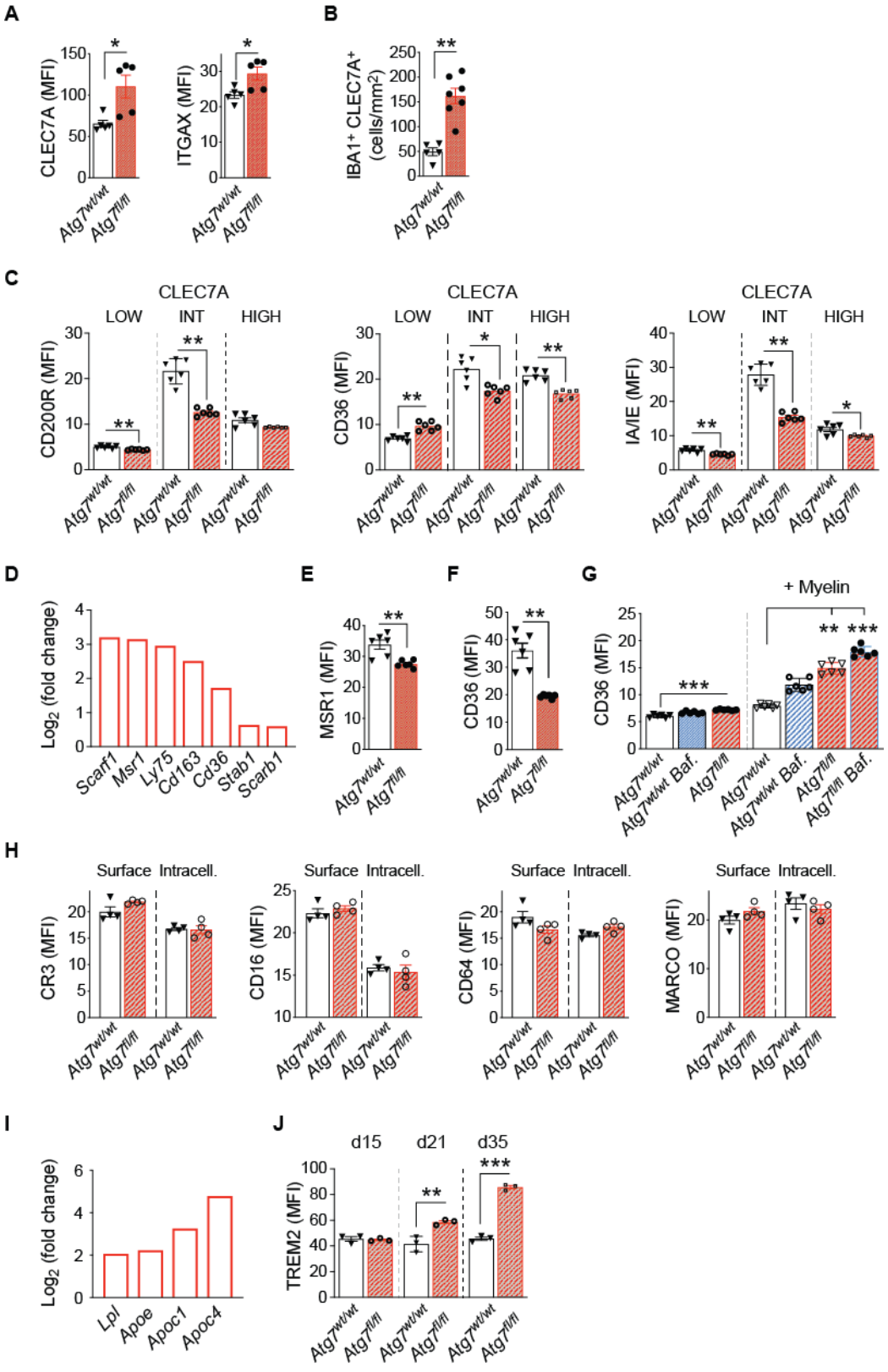

Fig. S6. *Atg7* deficient microglia have impaired scavenger receptor recirculation associated with increased inflammation and a reduced myelinating oligodendrocyte population in Experimental Autoimmune Encephalomyelitis (EAE).

(**A**) Flow cytometry quantification of surface CLEC7A and ITGAX (Cd11c) on *Atg7*$^{wt/wt}$*Cx3cr1*^{CreERT2} (*n* = 5) and *Atg7*$^{fl/fl}$*Cx3cr1*^{CreERT2} (*n* = 5) day 35 EAE microglia. (**B**) IBA1^{+}CLEC7A^{+} positive cells per mm^{2} in lesion area of central nervous system tissue day 32-37 after EAE induction of *Atg7*$^{wt/wt}$*Cx3cr1*^{CreERT2} (*n* = 5) and *Atg7*$^{fl/fl}$*Cx3cr1*^{CreERT2} (*n* = 7). (**C**) Flow cytometry assessment of surface CD200R, CD36 and IA/IE in *Atg7*$^{wt/wt}$*Cx3cr1*^{CreERT2} (*n* = 6) and *Atg7*$^{fl/fl}$*Cx3cr1*^{CreERT2} (*n* = 6) microglia populations defined by levels of CLEC7A expression as defined in Fig. 3, E and F. (**D**) Fold change increase of scavenger receptor mRNA expression in *Atg7*$^{fl/fl}$*Cx3cr1*^{CreERT2} (*n* = 4) compared to *Atg7*$^{wt/wt}$*Cx3cr1*^{CreERT2} (*n* = 3) microglia (RNA-sequencing, day 21 p.i., as in Fig. 2). Flow cytometry quantification of surface (**E**) MSR1 and (**F**) CD36 on *Atg7*$^{wt/wt}$*Cx3cr1*^{CreERT2} (*n* = 6) and *Atg7*$^{fl/fl}$*Cx3cr1*^{CreERT2} (*n* = 6) day 35 EAE microglia. (**G**) Flow cytometry quantification of intracellular CD36 from naïve Atg7wt/wt and Atg7fl/fl microglia exposed to myelin 12h in vitro w/wo 6h Bafilomycin A1 treatment. All conditions; n = 6. (**H**) Flow cytometry quantification of surface and intracellular density of scavenger receptors after 24h *in vitro* myelin exposure in *Atg7*$^{wt/wt}$*Cx3cr1*^{CreERT2} (*n* = 4) and *Atg7*$^{fl/fl}$*Cx3cr1*^{CreERT2} (*n = 4*) microglia sorted at day 5 p.i. (**I**) Fold change increase of lipoprotein mRNA expression in *Atg7*$^{fl/fl}$*Cx3cr1*^{CreERT2} (*n* = 4) compared to *Atg7*$^{wt/wt}$*Cx3cr1*^{CreERT2} (*n* = 3) microglia (RNA-sequencing, day 21 p.i., as in Fig. 2). (**J**) Surface density of TREM2 assessed with flow cytometry (*n* = 3 for all conditions). Statistics: Mann-Whitney U-test for all comparisons except (**G**) Kruskal–Wallis test followed by Dunn's post-hoc test and (**J**) Unpaired T-test (*** $p < 0.001$, ** $p < 0.01$, * $p < 0.05$). Error bars indicate SEM. Experiments (**A**) were repeated three times and experiments (**C**, **E** to **H**, and **J**) were repeated twice.

Supplementary Figure 7

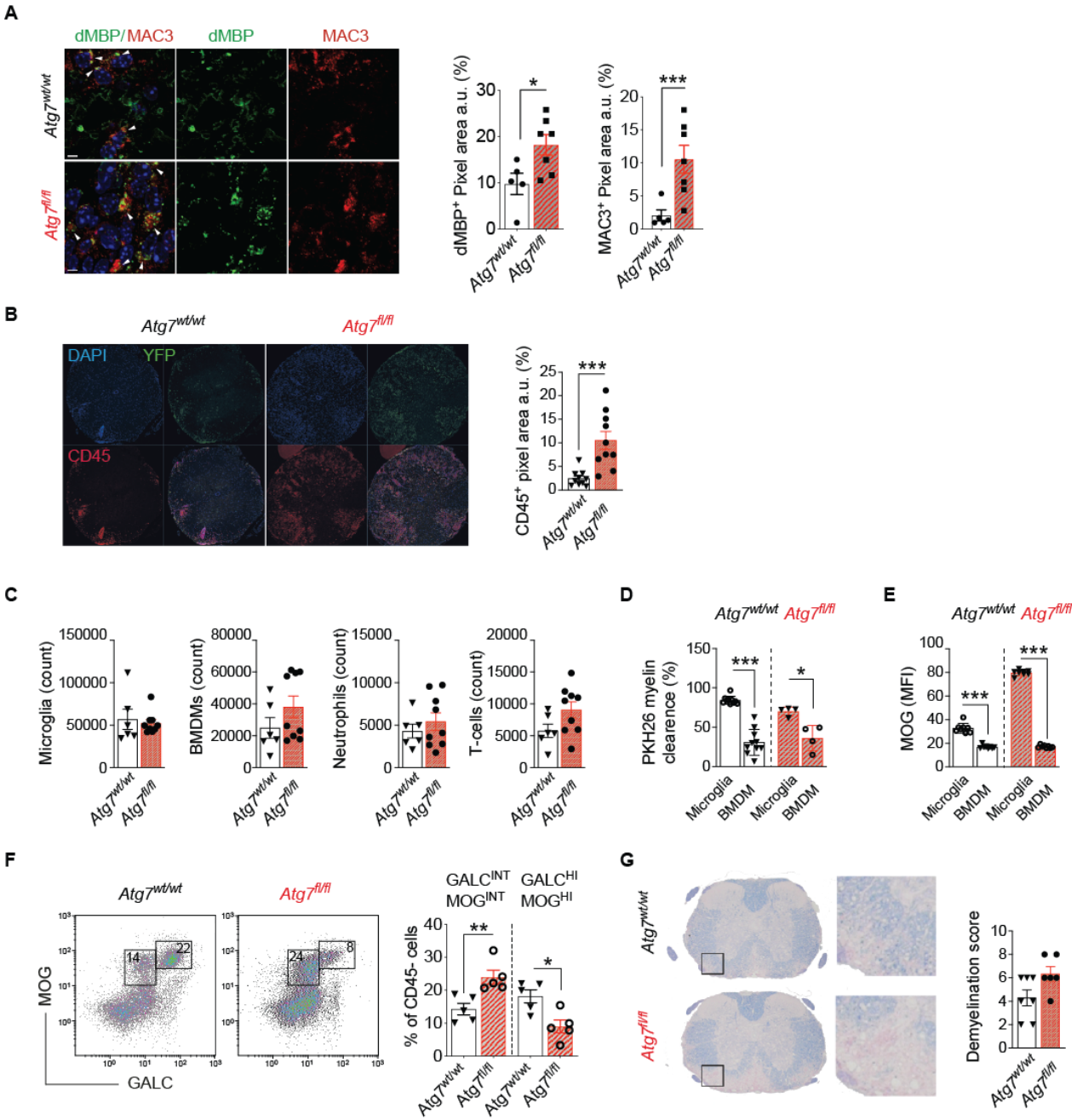

Fig. S7. Late stage Experimental Autoimmune Encephalomyelitis (EAE) is characterized by extensive tissue destruction and signs of increased inflammation in mice with *Atg7*-deficient microglia.

(**A**) Zoomed images and immunofluorescence quantification (as in Fig. 3N) of tissue deposits of myelin debris (dMBP) and density of $MAC3^+$ macrophages at day 32-40 p.i. in spinal cord from *Atg7*$^{wt/wt}$*Cx3cr1*^{CreERT2} (dMBP, n = 5; MAC3, n = 10) and *Atg7*$^{fl/fl}$*Cx3cr1*^{CreERT2} mice (dMBP, n = 7; MAC3, n = 10). DAPI defines nuclei. (**B**) Immunofluorescence depicting $CD45^+$ cells and YFP^+ microglia in spinal cord from mice day 32-40 p.i. $CD45^+$ pixel area quantified from three pooled experiments (n = 10 per group). (**C**) Infiltrating immune cells and microglia from spinal cord of *Atg7*$^{wt/wt}$*Cx3cr1*^{CreERT2} (n = 6) and *Atg7*$^{fl/fl}$*Cx3cr1*^{CreERT2} (n = 9) mice at day 35 p.i. assessed by flow cytometry. Counts indicate numbers of microglia and infiltrating immune cells (bone marrow derived macrophages (BMDM), $Ly6G^+$ neutrophils and $CD3^+$ T-cells). (**D**) *In vitro* myelin clearance assay of day 35 sorted central nervous system myeloid cells pulsed 3 times with PKH26 labeled myelin (*Atg7*$^{wt/wt}$*Cx3cr1*^{CreERT2}; n = 10, *Atg7*$^{fl/fl}$*Cx3cr1*^{CreERT2}; n = 4). (**E**) Flow cytometry detection of intracellular MOG in *ex vivo* stained microglia and BMDM at day 35 p.i. (n = 9 per group). (**F**) Flow cytometry detection of cells from the oligodendrocyte lineage 30 days p.i. Percentage of $CD45^-GALC^+MOG^+$, reflecting a myelinating population, in *Atg7*$^{fl/fl}$*Cx3cr1*^{CreERT2} (n = 5) and *Atg7*$^{wt/wt}$*Cx3cr1*^{CreERT2} (n = 5) mice. (**G**) Representative images of the spinal cord stained with Luxol fast blue showing reduced myelination in the *Atg7*$^{fl/fl}$*Cx3cr1*^{CreERT2} spinal cord during days 27-40 p.i. Graph showing demyelination scores in *Atg7*$^{fl/fl}$*Cx3cr1*^{CreERT2} (n = 6) compared to *Atg7*$^{wt/wt}$*Cx3cr1*^{CreERT2} (n = 7) mice. Statistics: Mann-Whitney U-test for all comparisons (*** $p < 0.001$, ** $p < 0.01$, * $p < 0.05$). Error bars indicate SEM. Experiments (**D** and **E**) were performed twice and (**C** and **F**) three times.

Supplementary Figure 8

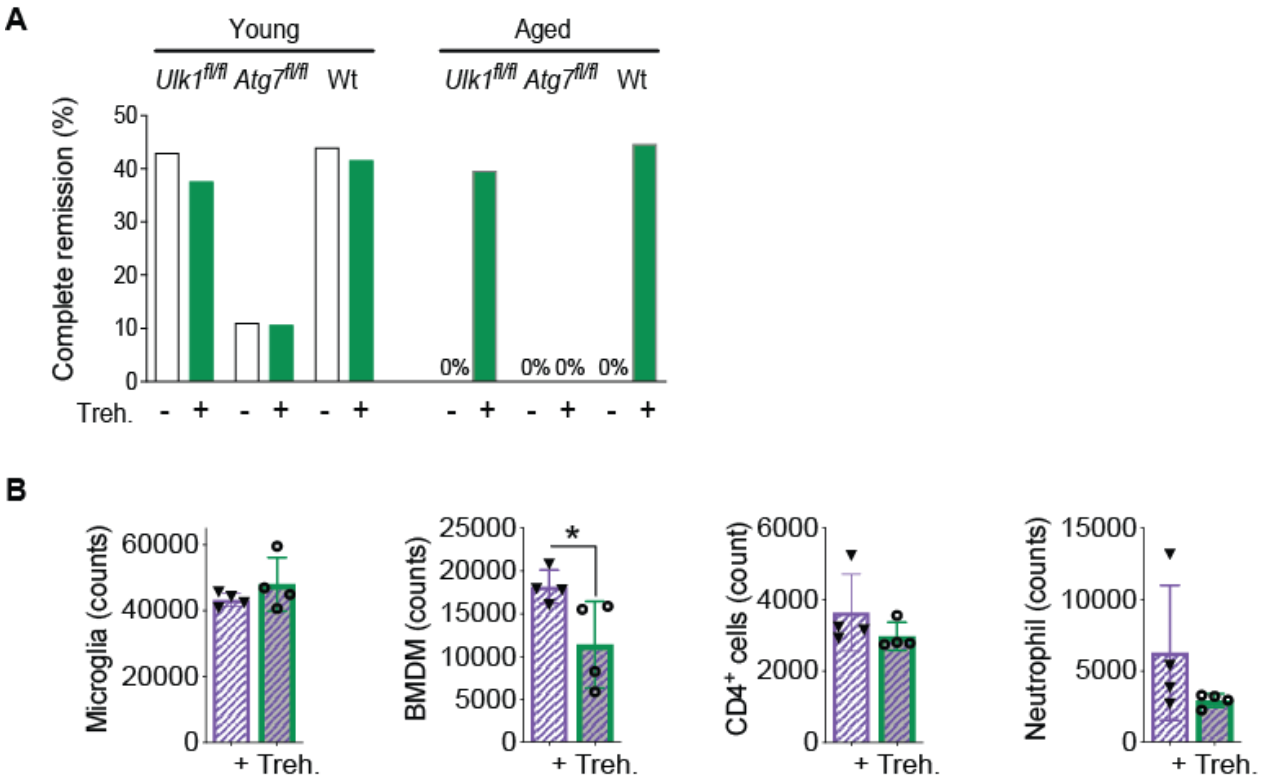

Fig. S8. Trehalose boosts Experimental Autoimmune Encephalomyelitis (EAE) recovery and decreases immune infiltration in aged mice.

(**A**) EAE recovery rate in young (12-22 weeks old), *Atg7*$^{wt/wt}$*Cx3cr1*^{CreERT2} (control; *n* = 11, treated; *n* = 11), *Ulk1*$^{fl/fl}$*Cx3cr1*^{CreERT2} (control; *n* = 7, treated; *n* = 9) and *Atg7*$^{fl/fl}$*Cx3cr1*^{CreERT2} (control; *n* = 9, treated; *n* = 9) mice and aged *Atg7*$^{wt/wt}$*Cx3cr1*^{CreERT2} (control; *n* = 4, treated; *n* = 6), *Ulk1*$^{fl/fl}$*Cx3cr1*^{CreERT2} (control; *n* = 4, treated; *n* = 5) and *Atg7*$^{fl/fl}$*Cx3cr1*^{CreERT2} (control; *n* = 5, treated; *n* = 5) mice. Mice were treated with Trehalose or water control. (**B**) Infiltrating immune cells and microglia from spinal cord of aged mice (*n* = 4) and Trehalose treated aged mice (*n* = 4) at day 21 p.i. assessed by flow cytometry. Statistics: Mann-Whitney U-test for all comparisons (* $p < 0.05$). Error bars indicate SEM. Experiments (**A** and **B**) were performed twice.

Supplementary Figure 9

Gating strategy for defining cell populations by Flow cytometry